RICE UNIVERSITY

Nonlinear Optical Properties of Highly Aligned Carbon Nanotubes

by

Darius T Morris, Jr.

A Thesis Submitted
in Partial Fulfillment of the
Requirements for the Degree

Master of Science

Approved, Thesis Committee:

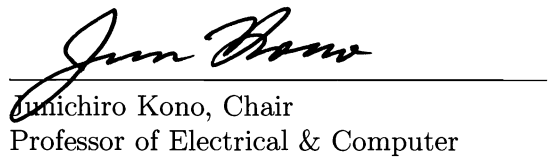

Junichiro Kono, Chair
Professor of Electrical & Computer Engineering and Physics & Astronomy

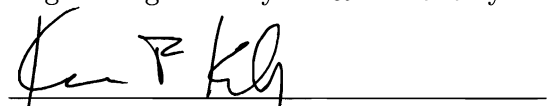

Kevin F. Kelly
Associate Professor of Electrical & Computer Engineering

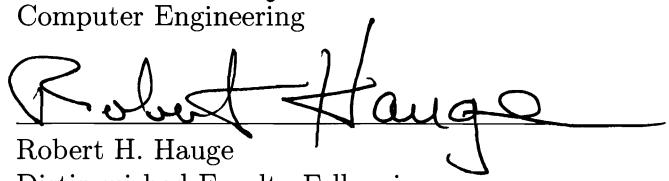

Robert H. Hauge
Distinguished Faculty Fellow in Chemistry

Houston, Texas

April, 2011

ABSTRACT

Nonlinear Optical Properties of Highly Aligned Carbon Nanotubes

by

Darius T Morris, Jr.

Through polarization-dependent third hamonic generation experiments done on highly aligned carbon nanotubes on sapphire, the nonzero tensor elements of $\chi^{(3)}$ have been extracted. The contribution of the weaker tensor elements to the overall $\chi^{(3)}$ signal has been calculated to be approximately 1/3rd of that of the dominant $\chi^{(3)}_{zzzz}$ component, which is consistent with theory and other measured values.

Acknowledgments

I would first like to thank my Lord and Savior, Jesus Christ for giving me strength, guidance, and peace. Through Him I know that all things are possible.

I would also like to thank my mom, dad, sister and the rest of my family. These are the people from whom I draw my inspiration. Thank you for your unconditional love and keeping in your prayers.

Thank you to Dr. Kono for giving me opportunity to work in your lab and travel to other countries to do research. Thank you for always taking time out of your busy schedule to address any experiment issues or for any impromptu physics lessons. Also, thanks to my committee for coming together at the last minute so that I can defend my masters, for your patience through the defense process.

Thank you to my colleagues in Kono Lab for your endless support in the laboratory environment and for your insight on experimental methods. If there was anything that I needed, you all made time to address those questions. You are a unique group that makes grad school bearable when experiments aren't working.

Thanks to my collaborators for taking interest in my research and for having the patience to see me through every experiment.

I would like to also thank all of my funding agencies, especially MIRTHE for providing the extra knowledge and opportunities that I gained from the workshops, presentations, and retreats. Special thanks to Roxanne for making sure that I get to/from those destinations and that I have a place to stay, no matter the mishap.

Thanks to Sarah, Yvonne, Joan and any other Kono Lab staff who helped with

the school/personal issues that came up in graduate school, and for making sure my money is right. I would also like to thank Theresa Chatman and the AGEP program for their constant support, and making sure that I get fed.

Last but not least, to my friends that I had before graduate school and the ones that I've made while I was here. Thanks for keeping me entertained on a daily basis, keeping me up on music, sports, politics, and entertainment, when lab doesn't permit me to do so. Thank you for always lending an ear when things in my life dont go the way that they are supposed to, and making me laugh when I needed it. Thank you to my girlfriend, Jasmine Brown, for understanding the life of a graduate student, being supportive, and being in love with me (even though you haven't said it yet, I know you do).

Contents

Illustrations

Chapter 1

Introduction

Over the past 80 years, a vast amount of theoretical and experimental research has been done on carbon based materials, giving rise to some fascinating optical, electrical, and mechanical properties. Graphene, which can be described as a 2-dimensional hexagonal lattice of sp^2 bonded carbon atoms, is the fundamental building block of these carbon based materials. Conceptually, graphene can be balled up into 0D, fullerenes, rolled into 1D carbon nanotubes (CNTs), and stacked into 3D graphite, as seen in Figure 1.1.

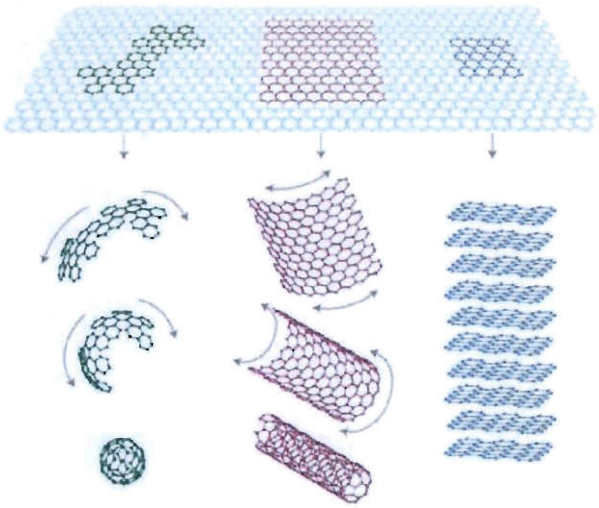

Figure 1.1 : 2D graphene and its derivatives, (a) 0D fullerenes, (b) 1D carbon nanotubes, and (c) 3D graphite [1].

Due to its conical dispersion relation near the k points at the six corners of the first Brillouin zone, electrons behave like massless Dirac fermions, possessing a high fermi velocity (v_F 10^6m/s), high electron mobility (200,000$\frac{cm^2}{Vs}$), and minimum conductivity, despite zero carrier density near the Dirac point. This linear energy dipersion also leads to a universal optical conductivity, $\pi e^2/2h$, in which each atomic layer of graphene absorbs 2.3% of incident light from the visible to the far-infrared [1] [2]. These unique electrial and optical properties have also trickled down to graphene's various derivatives, making them great candidates for a wide variety of potential applications, like transistors, capacitors, and detectors [3] [4] [5] [6] [7] [8]. CNTs, in particular, depending on the way they are rolled up, display various optical and electrical properties, most of which have been investigated in hundreds of studies. CNTs have been measured to have a fermi velocity of v_F 8.1×10^5m/s, a measured electron mobility of 100,000$\frac{cm^2}{Vs}$, and an ability to absorb light from the visible to the THz. Though a lot of work has been done on the electrical and optical properties of CNTs, only, a small amount of studies have been done on the nonlinear optical properties of CNTs. This thesis is concerned with exploring the second and third order harmonic processes in CNTs.

Chapter 2

Band Structure and Linear Optical Properties of Semiconducting Carbon Nanotubes

2.1 Single-walled carbon nanotubes

Carbon nanotubes can be pictured as a single sheet of graphene rolled at a particular angle along the axis perpendicular to its long axis (tube axis), as seen in Figure 2.1. This perpendicular axis points along the direction of the chiral vector $\vec{C}_h$, defined as

$$\vec{C}_h = m\vec{a}_1 + n\vec{a}_2, \tag{2.1}$$

where $\vec{a}_1$ and $\vec{a}_2$ are unit vectors at $60\,^\circ$ angles to each other, which define the unit cell of graphene in real space, and are defined as

$$\vec{a}_1 = \left(\frac{\sqrt{3}}{2}a, \frac{a}{2}\right) \text{ and } \vec{a}_2 = \left(\frac{\sqrt{3}}{2}a, -\frac{a}{2}\right). \tag{2.2}$$

Thus, many types of CNTs can be conceptualized via the chiral index (n, m). There are three main types of CNTs: Zigzag ($m = 0$), armchair ($n = m$), and chiral ($n \neq m$ and $m \neq 0$).

The 1D energy dispersion relation for CNTs is derived from the 2D band structure of graphene, using the zone-folding method. This 2D energy dispersion relation of graphene can be derived by solving the eigen-value problem for a Hamiltonian, $H_{G,2D}$ associated with the two carbon atoms in the graphene unit cell, within the tight-binding approximation, defined as

$$H_{G,2D} = \begin{bmatrix} 0 & f(k) \\ -f^\dagger(k) & 0 \end{bmatrix}, \tag{2.3}$$

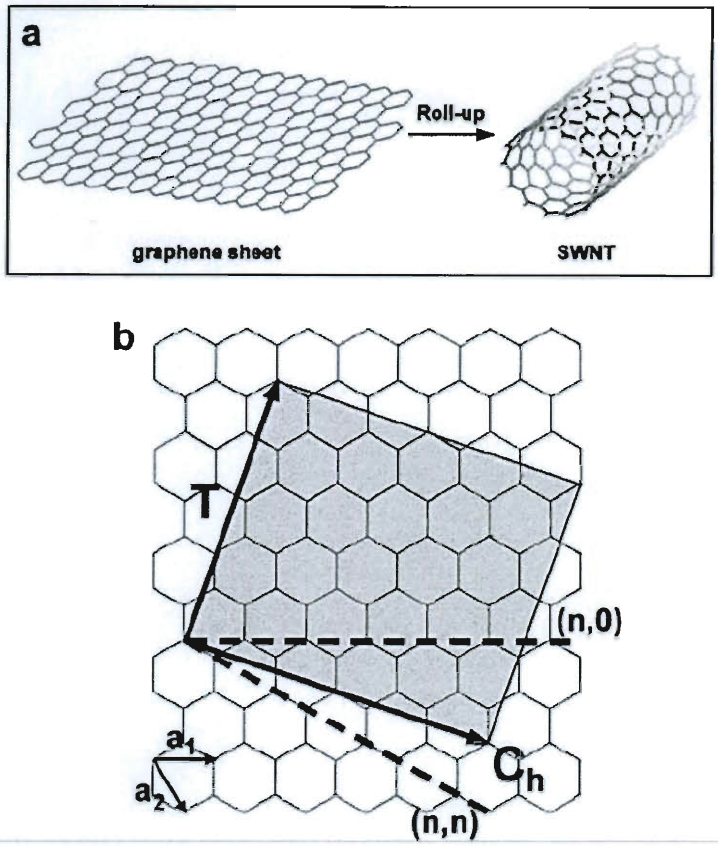

Figure 2.1 : (a) Conceptually, CNTs are 1D cylindrical sheets of graphene, (b) rolled along chrial vector C_h [9].

where $f(k) = -\gamma(1 + e^{i\vec{k}\cdot\vec{a_1}} + e^{i\vec{k}\cdot\vec{a_2}})$ and γ is the nearest neighbor C-C tight binding overlap energy. In this two carbon basis, the electrons in this system move as planar Bloch waves. The solution for the eigenvalue equation $|H_{G,2D} - EI = 0|$ leads to the energy dispersion relation for the 2D graphene, shown in figure (2.2),

$$E^{\pm}_{G,2D}(k) = \pm\gamma\sqrt{1 + 4\cos\frac{\sqrt{3}k_x a}{2}\cos\frac{k_y a}{2} + \cos\frac{k_y a}{2}}, \tag{2.4}$$

where $\gamma = 2.7$eV, and $\pm$ denotes the upper and lower π energy bands.

Using the zone folding method, the wavefunctions must be subject to periodic

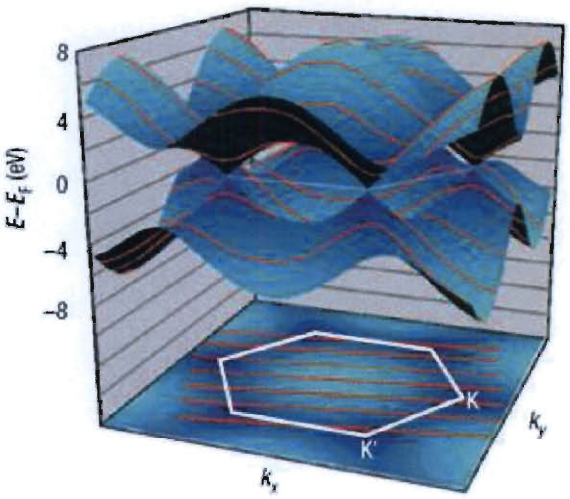

Figure 2.2 : Calculated 2D energy dispersion for graphene. [10].

boundary conditions, and are quantized along the cylindrical direction. And the energy dispersion relation for SWNTs becomes

$$E_{1D}^{\pm} = E_{G,2D}^{\pm}(k\frac{\vec{K_2}}{\left|\vec{K_2}\right|} + \mu\vec{K_1}), \text{ where } \mu = 0, 1, ..., N-1, \tag{2.5}$$

where μ is the zone-folding index, and $\vec{K_1}$ and $\vec{K_2}$ are reciprocal lattice unit cell vectors as shown in Figure 2.3. Thus, if the SWNT is rolled in such a way that the allowed k values land on the K or K' point of graphene, then the CNT is metallic ($|m-n|$ mod $3 = 0$). Otherwise the tubes are semiconducting S1 ($|m-n|$ mod $3 = 1$) or S2 ($|m-n|$ mod $3 = 2$), whose band gap can also be determined, by subtracting the energies of the upper and lower π bands at $k = 0$.

$$E_g = \frac{2\gamma_0 a_{c-c}}{d} \tag{2.6}$$

where γ_0 is the overlap energy, a_{c-c} is the inner atomic distance, and d is the diameter.

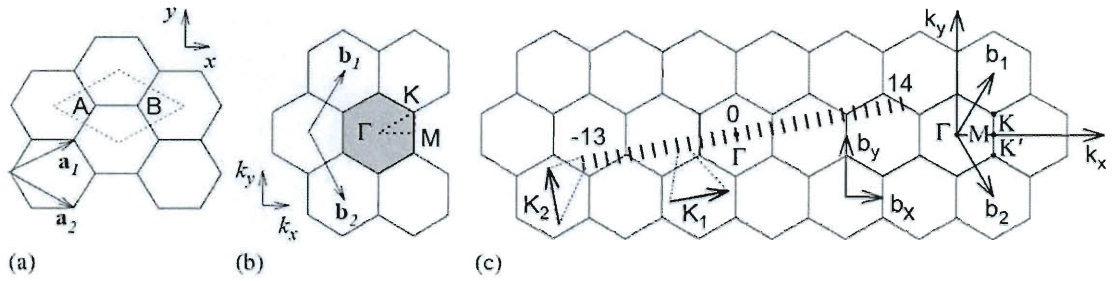

Figure 2.3 : Unit vectors in and primite cell (a) in real space and (b) reciprocal space. (c) Zone folding in (4,2) nanotube [11].

The energy dispersion relations for metallic and semiconducting tubes can be seen in Figure 2.4.

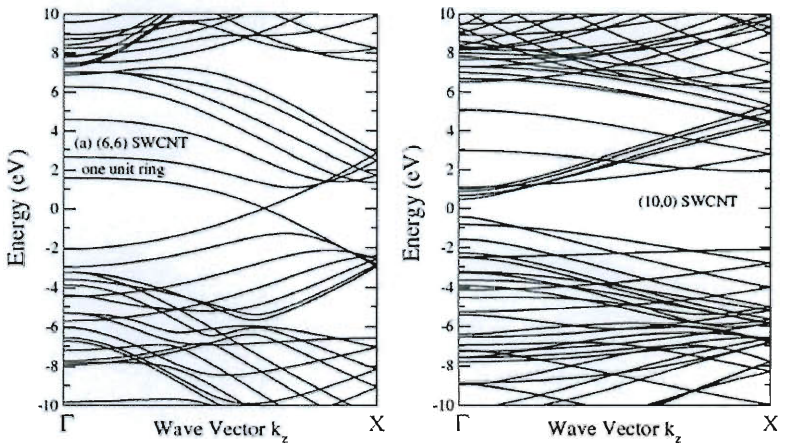

Figure 2.4 : 1D energy dispersion for the(a) metallic (6,6) armchair nanotube, (b) and the semicoducting (10,0) zigzag nanotube [12].

2.2 Linear optical properties of SWNTs

CNTs have a very large aspect ratio, with a diameter on the order of nanometer, but have been grown as long as 4 cm. Many of the features of the linear optical properties of CNTs are attributed to their quasi 1D density of states. The dispersion relation for isotropic, linear (p=1) and parabolic (p=2), energy bands can be expressed as

$$E = E_0 + c_k k^p \Rightarrow k = \left(\frac{E - E_0}{c_k}\right)^{1/p} \tag{2.7}$$

The volume of a 1-dimensional k-space containing wave vectors smaller than k is

$$\Omega_1(k) = 2k \Rightarrow \Omega_1(k) = 2\left(\frac{E - E_0}{c_k}\right)^{1/p}, \tag{2.8}$$

thus, the density of states for the 1D dispersion relation is

$$D_1(E) = \frac{2}{pc_k^{1/p}}(E - E_0)^{\frac{1}{p-1}} \tag{2.9}$$

For metallic SWNTs, electrons behave like Dirac fermions due to the linear (p=1) dispersion relation near the Dirac point. Thus, its density of states is constant, $D_{1,lin}(E) = 1/c_k$, near the dirac point. And for semiconducting SWNTs, electrons have a parabolic dispersion relation near the k=0 point, thus the density of states is $D_{1,para}(E) = \frac{1}{2\sqrt{c_k(E-E_0)}}$. As you can see, the density of states possesses sharp peaks, called van Hove singularities. Metallic tubes also show these van Hove singularities, due to the bending of the π energy band away from the Dirac point, as shown in Figure 2.6.

These van Hove singularities give rise to optical transitions in nanotubes between the valence and conduction bands. Many of these transitions, specifically the semiconducting S_{11} and S_{22}, and metallic M_{11} transitions, have been studied using absorption, photoluminescence, and Raman spectroscopy experiments. These optical transitions are strong and sharp, allowing scientists to probe a single type of tube in these various

experiments. These transitions can also be tuned changing the diameter (determines band gap) of the tubes, see Figure 2.5.

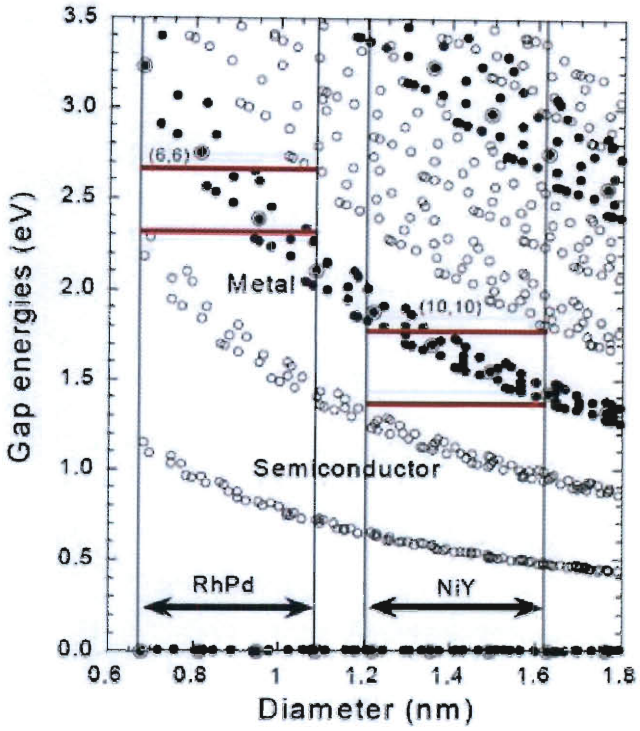

Figure 2.5 : Kataura plot showing the decrease in transition energy with increasing diameter of the nanotubes [13].

In absorption experiments, the van Hove singularities are evident due to the sharp features that appear in a typical absorption experiment. Gaining information about a particular type of tube is difficult, however, because serveral tubes have similar diameters, and thus, absorption energies across bandgap can be the same, when you have a collection of SWNTs, as seen in Figure 2.6.

Instead of using absorption to characterize nanotubes, many groups study luminescence in nanotubes, because most nanotubes have a unique set of S_{11} and S_{22}

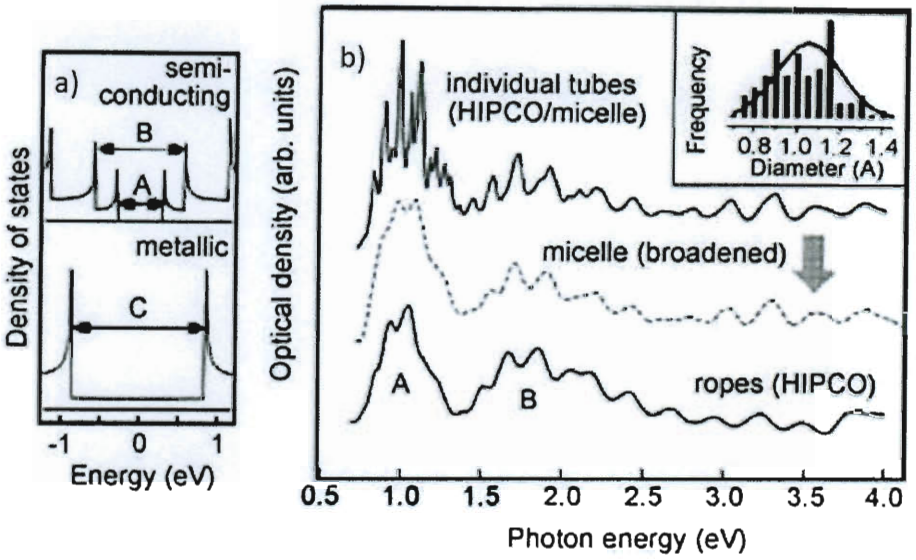

Figure 2.6 : (a) 1D density of states for metallic and semiconducting nanotubes. (b) Optical density (absorption) measured for carbon nanotubes suspended in different serfactants [14].

transitions. In a photoluminescence experiment, an electron-hole pair called an exciton is created, after an electron is absorbed at the S_{22} energy, both the electron and hole relax down to the c_1 and v_1 energy levels and then recombine, creating a photon at the S_{11} energy [15]. This process is often used to characterize a sample containing a plurality of nanotubes, as seen in Figure 2.7. It is, however, a very inefficient process, and does not happen in metallic tubes (created hole immediately filled by electron in metal, thus no recombination).

Raman scattering, shown in Figure 2.8 is the most popular characterization technique for nanotubes. It has a very large sensitivity and can offer much information about the nanotubes. After being resonantly excited, several modes can be measured from the subsequent Raman spectra, like the radial breathing, G, D, and G' modes. Stokes and anti-Stokes scattering can be used to further characterize semiconduct-

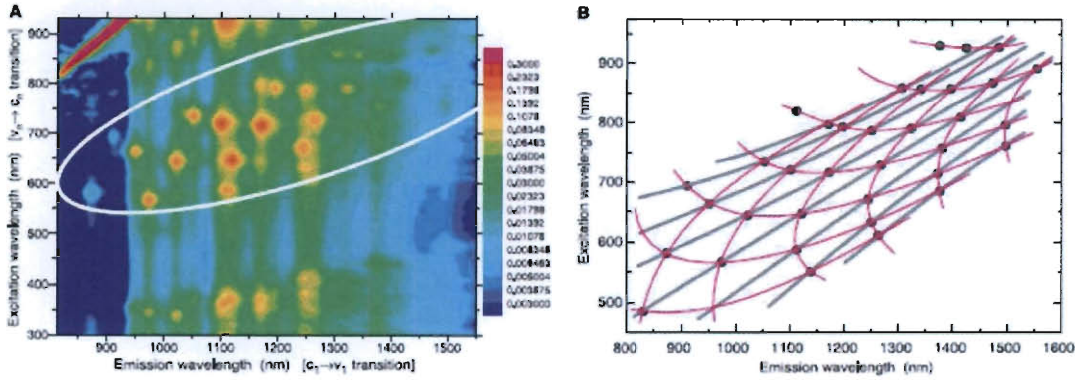

Figure 2.7 : (a) PLE map from sample containing many chirality of tubes. (b)Shows spectral peak positions from the PLE map, with lines that show perceived patterns in the data [16].

ing nanotubes, where the S_{22} energy transition is redshifted for $S1$ nanotubes and blueshifted for $S2$ nanotubes, with increasing temperature.

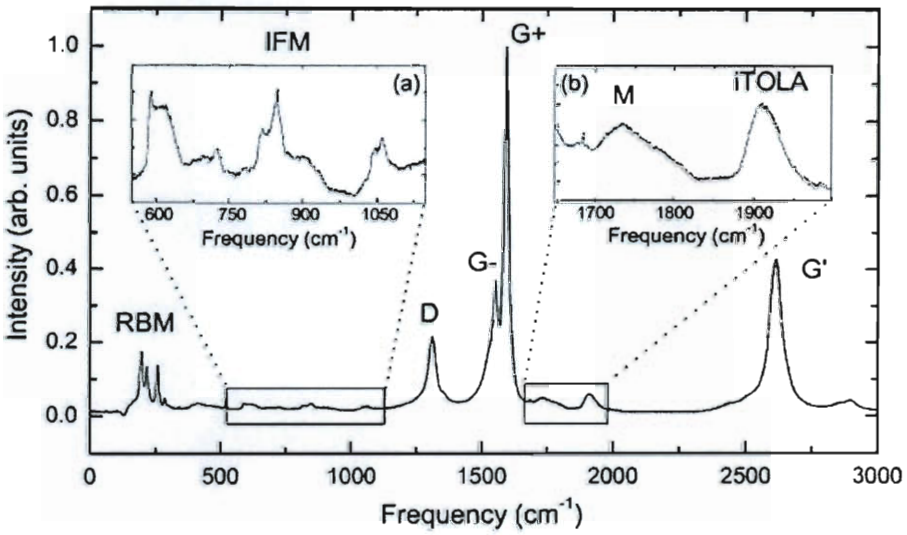

Figure 2.8 : Typical Raman spectrum from HiPco nanotube sample obtained with excitation energy $E_L = 1.96$eV, illustrating the radial breathing, G, D, and G' modes, as well as the intermediate-frequency modes adn iTOLA bands in the insets. [17].

Chapter 3

Basics of Nonlinear Optics

3.1 What is nonlinear optics?

When light is incident on a dielectric material, the electric field components, transverse to the propogation direction, displaces the electrons present in the material. The eletrons propogate back and forth, like a spring, around a positve charge, creating a dipole moment in the material. This dipole moment per unit volume is known as the polarization. The polarization in the material can be decribed by the following relationship:

$$\tilde{P}(t) = \chi^{(1)}\tilde{E}(t) + \chi^{(2)}\tilde{E}^2(t) + \chi^{(3)}\tilde{E}^3(t) + ... \quad (3.1)$$

$$\equiv \tilde{P}^{(1)}(t) + \tilde{P}^{(2)}(t) + \tilde{P}^{(3)}(t) + ... \quad (3.2)$$

where $\chi^{(1)}$, $\chi^{(2)}$, and $\chi^{(3)}$ are the optical susceptibilities of the material system [[18]]. The first term on the right hand side of the equation, the linear polarization in the material depends linearly on the stregth of the applied electric field. Conventional, or linear, optics, is the study of $\tilde{P}^{(1)}(t)$ effects, like absoption, refraction, etc. If the induced polarization depends nonlinearly on the applied electric field strength, then effects are explored in, nonlinear optics.

3.2 Nonlinear optical susceptibilities

The nonlinear susceptibilities, mentioned in section 3.1, give all the information needed to know about the nonlinear response of a material system. If we consider the

vector nature of the electic field, $\chi^{(2)}$ becomes a third-rank tensor, while $\chi^{(3)}$ becomes a fourth-rank tensor, whose tensor elements serve as constants of proportionality between the nonlinear polarization to the product of E field amplitudes, as shown in the relationships below.

$$P_i(\omega_n + \omega_m) = \sum_{jk} \sum_{(nm)} \chi^{(2)}_{ijk}(\omega_n + \omega_m, \omega_n, \omega_m) E_j(\omega_n) E_k(\omega_m) \tag{3.3}$$

and

$$P_i(\omega_o+\omega_n+\omega_m) = \sum_{jkl} \sum_{(mno)} \chi^{(3)}_{ijkl}(\omega_o+\omega_n+\omega_m, \omega_o, \omega_n, \omega_m) E_j(\omega_o) E_k(\omega_n) E_k(\omega_m) \tag{3.4}$$

Due to the many nonlinear processes that take place in materials, there are several nonlinear tensors and tensor elements that can be conceptualized for describing a particular interaction. Each of these tensors has various symmetry properties that simplify calculations, like intrinsic permutation symmetries, symmetries for lossless media, Kleinman's symmetry, and spatial symmetries. Specifically, if a material is centrosymmetric, or posesses inversion symmetry, the nonlinear $\chi^{(2)}$ response goes to zero[[19]].

3.3 Second-order nonlinear optical processes

Second-order nonlinear optical properties are present in noncentrosymmetric crystals. If we consider an electric field with 2 distict electric field components, ω_1 and ω_2 represented by $\tilde{E}(t) = E_1 e^{-i\omega_1 t} + E_2 e^{-i\omega_2 t} + c.c.$ incident on a medium with nonlinear suscepitibility $\chi^{(2)}$, the second order nonlinear polarization is given by

$$\tilde{P}^{(2)}(t) = \chi^{(2)} \tilde{E}(t)^2 \tag{3.5}$$

$$= \chi^{(2)} \left[E_1^2 e^{-2i\omega_1 t} + E_2^2 e^{-2i\omega_2 t} + 2E_1 E_2 e^{-i(\omega_1+\omega_2)t} + 2E_1 E_2^* e^{-i(\omega_1-\omega_2)t} + c.c. \right] \tag{3.6}$$

$$+2\chi^{(2)}[E_1 E_1^* + E_2 E_2^*]. \tag{3.7}$$

Each of these terms on the right side of Equation 3.7 corresponds to a 2nd order nonlinear process. The first 2 terms of the nonlinear polarization has frequency components, $2\omega_1$ and $2\omega_2$, at twice the frequencies of the input fundamentals. This process is called second harmonic generation (SHG), in which two photons of frequency ω are detroyed to create a photon at twice the frequency, 2ω, shown in Figure 3.1a. Other processes are also present in this nonlinear polarzation, like sum frequency generation ($\omega_1 + \omega_2$, SFG), in which a photon is created at a frequency equal to the sum of the input frequncies. Similarly, a photon can be created at frequency equal to the differnce of the input frequncies ($(\omega_1 - \omega_2)$). This process is called difference frequency generation (DFG). Both processes are shown in Figures 3.1b and 3.1c. The last term refers to optical rectification, in which a static field, with no time component, is created.

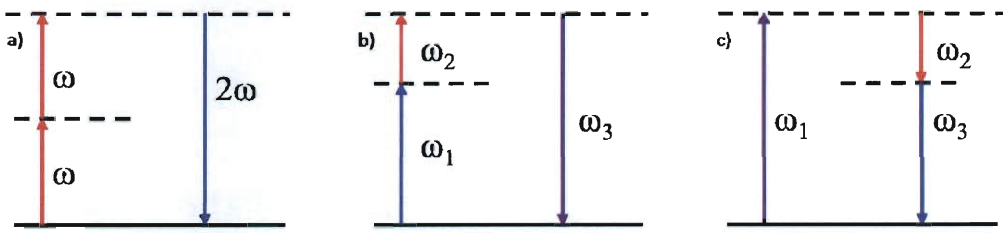

Figure 3.1 : Illustration of second order nonlinear processes (a) SHG (b) SFG, and (c) DFG [18].

3.4 Third-order nonlinear optical processes

Third-order nonlinear optical properties are present in all crystal types (lowest observable nonlinear process in centrosymmetric crystals). Similar to the calculations presented in section 3.3, the frequency components of these 3rd order nonlinear processes can be understood. In third harmonic generation, 3 photons of the same frequency are destroyed to create a photon at 3 times the frequency of the incident

fundamental beam. Four wave mixing is a process in which three photons of different frequencies mix (various combinations of created and destroyed input photons), to create a photon whose frequency is equal to the sum and/or difference of the 3 input frequencies. As shown in Figure 3.2b.

One term that arrises when calculating the third-order polarization is

$$P^{(3)}(\omega) = 3\chi^{(3)}(\omega = \omega + \omega - \omega) \left|E(\omega)^2\right| E(\omega). \tag{3.8}$$

From this equation, we see that there is a part of the nonlinear polarization that influences the propogation of the fundamental frequency ω. This term effectively describes the intensity dependent index of refraction, n_2 in the equation below of the refractive index in the presence of a nonlinear environment.

$$n \equiv n_0 + n_2 I, \text{ where } n_2 = \frac{12\pi^2}{n_0^2 c}\chi^{(3)} \tag{3.9}$$

This nonlinear refractive index leads to self focusing, seen in Figure 3.2c of the fundamental in a material system. The imaginary part of this complex nonlinear index of refraction is used to describe intensity dependent (saturable) absorption, β, in the equation below.

$$\beta = \frac{\beta_0}{1 + I/I_s} \tag{3.10}$$

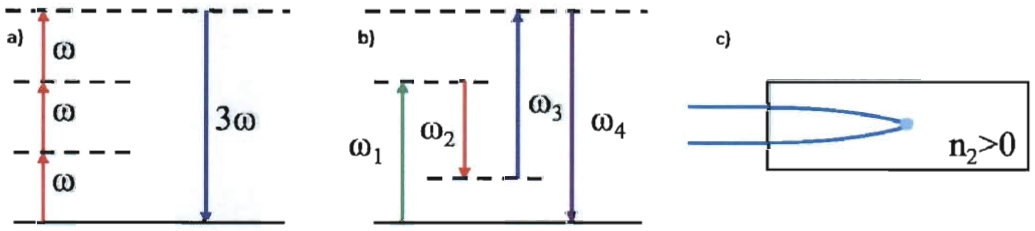

Figure 3.2 : Illustration of third order nonlinear processes (a) THG (b) four wave mixing, and (c) nonlinear index of refraction, which causes self focusing [18].

Chapter 4

Prior Nonlinear Optical Studies of Single-Walled Carbon Nanotubes

4.1 Theoretical work

There have been very few successful attempts to experimentally observe the nonlinear optical properties of CNTs. $\chi^{(2)}$ of the zigzag (m=0) and armchair (m=n) nanotubes does not exist because of their inversion symmetry, and the lack of inversion symmetry along the nanotubes axis in chiral nanotubes suggests that $\chi^{(2)}$ should be finite. Guo et al. theoretically reported that the nonzero tensor elements of the nonlinear susceptibility are χ_{xyz} and χ_{yzx}, and their relationship is $\chi_{xyz} = \chi_{yzx}$. They also calculated that the absolute value of $\chi^{(2)}$ is expected to be 10 times greater than that of GaAs, or 15^{-6} esu, illustrated in Figure 4.1. Guo et al. also suggested that, as the diameter of these tubes become larger, the absolute value of $\chi^{(2)}$ approaches zero, or that of graphene.

Third-order nonlinear optical properties of nanotubes have been investigated extensively by many groups, but different groups attain different values for the absolute value of $\chi^{(3)}$, and subsequent values that can be measured from nonlinear optical effects (i.e. nonlinear index of refraction). The relevant $\chi^{(3)}$ tensor elements that dominate the third-order susceptibility have also not be explored [21] [22] [23].

Theoretically, Margulis et al. used the Genkin-Mednis approach to calculate the nonlinear-optical spectra of $\chi^{(3)}$ for several third-order polarization effects, considering that the only interband and a combined interband/intraband motion of electrons

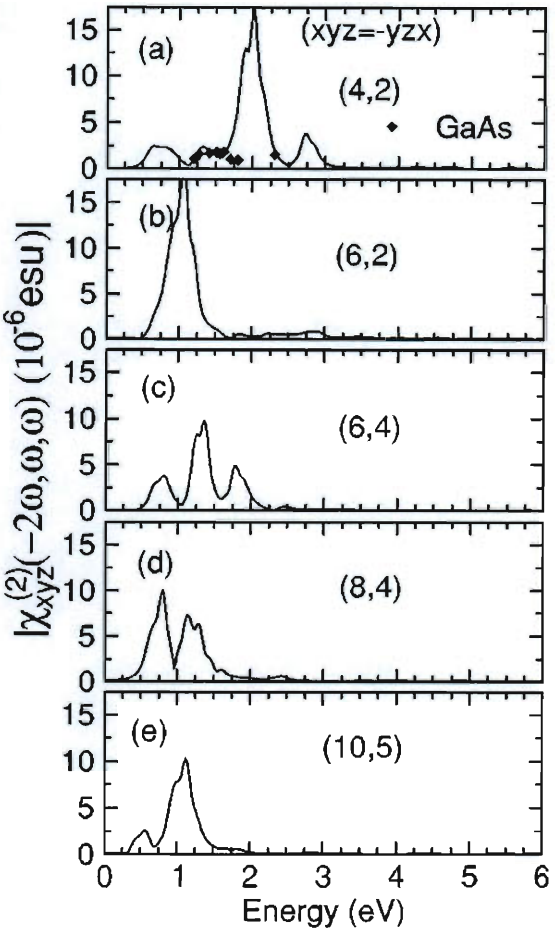

Figure 4.1 : Theoretical calculations of the absolute value of second order nonlinear susceptibility in chiral nanotubes, with measured values of GaAs (diamonds). When on resonance with the E11 transition, the absolute value is ten times that of GaAs [20].

contribute to the nonlinear optical response, of light polarized parallel to the long axis (z axis). From these calcuations they attained relationships for third harmonic generation, nonlinear index of refraction, two photon absorption, and the DC optical Kerr effect in carbon nanotubes, shown in Figures 4.2 and 4.3. For all of these effects, $\chi^{(3)}$ is significantly enhanced under on-resonance conditions. From these calcuations Magulis et al. reported an absolute value on the order of 10^{-8} to 10^{-6} esu for

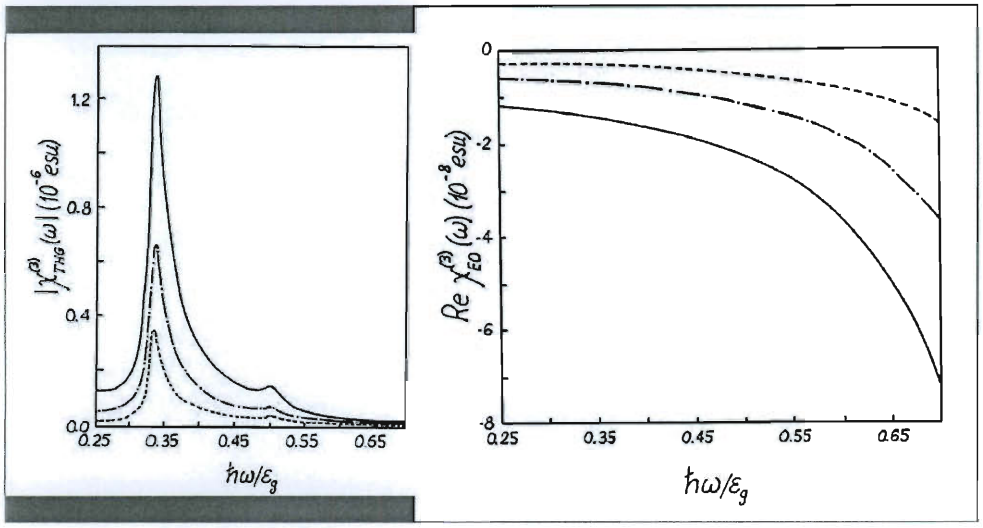

Figure 4.2 : Theoretical calculations of the absolute value of third order nonlinear susceptibility, for (a) THG and (b) optical kerr effet in nanotubes [24].

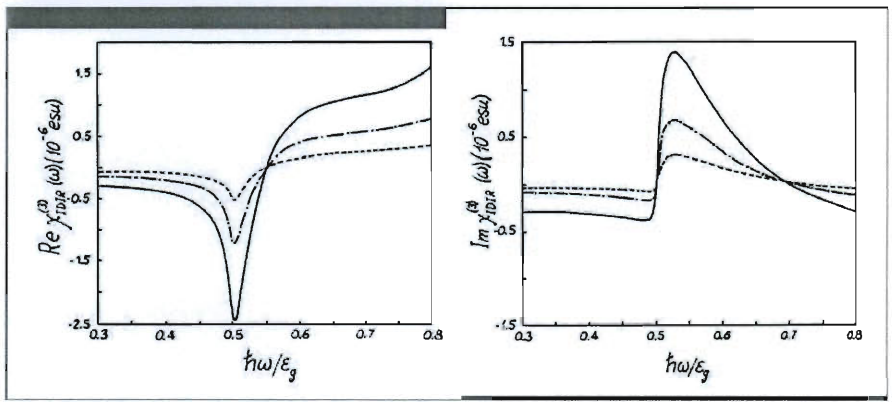

Figure 4.3 : Theoretical calculations of the (a) nonlinear index of refraction and (b) the two photon absorption coefficienct [24].

$\chi^{(3)}$ in carbon nanotubes, ($n_2 \approx 10^{-8}$ cm^2/W for the nonlinear refractive index, and $\beta \approx 10^{-5}$ cm/W for the two-photon absorption coefficient).

4.2 Experimental work

The absolute value of $\chi^{(2)}$ was experimentally confirmed by Su et al. in 2008 [25]. Experimentally, they measured resonant second harmonic generation from aligned SWNTs. Via Raman scattering, it was determined that only 3 types of nanotubes were present in the sample, the (5,0), the (3,3), and the (4,2), all of diameter 0.4 nm. Polarization dependent measurements were conducted, to confirm that the theoretically predicted tensor elements were indeed contributing to the overall $\chi^{(2)}$ signal as shown in Figure 4.4. Su et al. also observed a resonant enhancement in the second harmonic signal, at the expected E_{11} transition energy, measuring 2.1×10^{-6} esu for the absolute value of $\chi^{(2)}$, confirming the prediction by Guo et al.

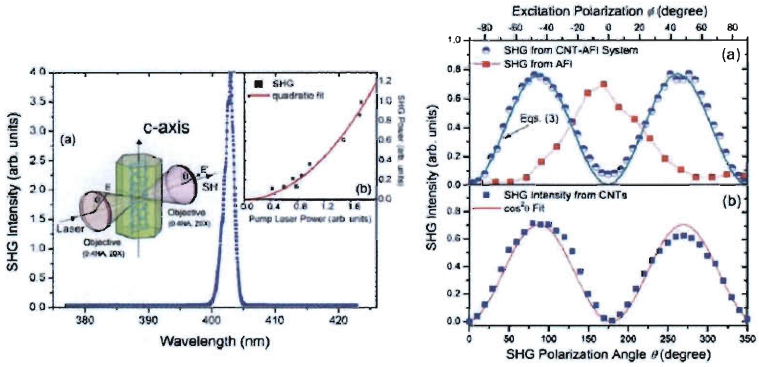

Figure 4.4 : (a) SHG produced from 800nm fundamental. (b) Power dependence of SHG relative to the input fundamental. Theta dependence of the (c) nanotubes with reference, reference, and (d) extracted nanotube contribution [25].

Several groups have observed third-order nonlinear optical properties from carbon nanotubes. Vivien et al. uses the z-scan method to measure the optical limiting properties of carbon nanotubes, specifically the nonlinear refractive index and the nonlinear absorption of the material [26]. By moving the sample along the propagation z-direction of a focused Gaussian beam, the focal spot position and far field intensity

of the Gaussian beam can change, due to self-focusing and self-phase modulation, from nonlinear scattering, nonlinear absorption (measured with an open aperture in the far field), and nonlinear index of refraction (measured with a closed aperture in the far field), shown in Figure 4.5. Vivien measures the z-scan transmittance for

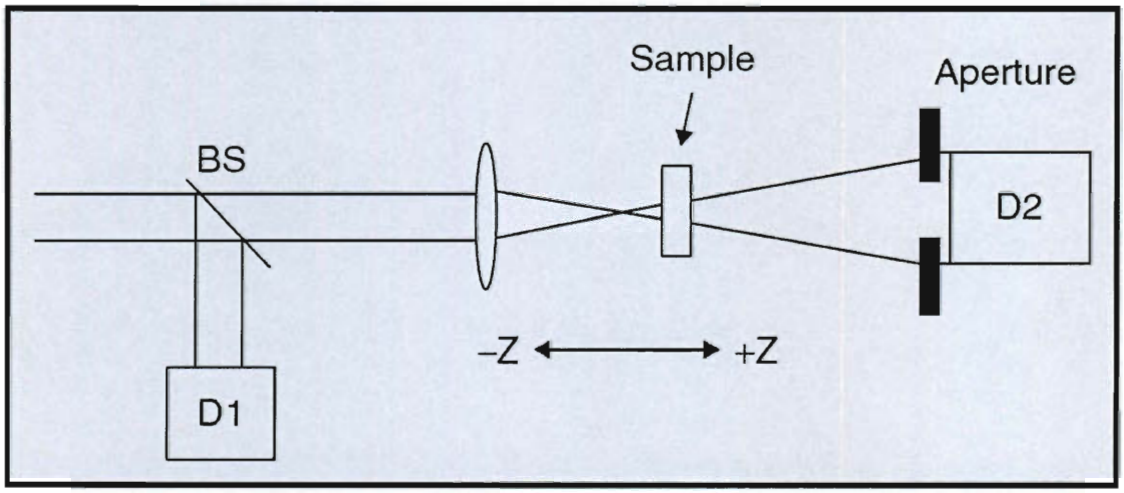

Figure 4.5 : Z-scan schematic for experimentally measuring the nonlinear index of refraction, and nonlinear absorption [27].

low/high powers and for closed/open apertures as seen in Figure 4.6. Experimentally, a values of $n_2 \approx -10^{-12}$ cm^2/W and $\beta \approx 5 \times 10^{-8}$ cm/W were obtained corresponding to a value of 10^{-10} esu for the value of $\chi^{(3)}$, which is three orders lower than other experimentally measured values (Muller et al. and Seo et al.) and four orders lower than Margulis et al.'s theory [28] [29].

Optical four wave mixing (OFWM) was also observed in SWNTs by several groups [30] [31]. In one experiment, by Kim, an ultrafast pump (omega pump) and Stokes (omega stokes) pulse pair excites the SWNT, and radiation from third-order electronic coherences is detected at the anti-Stokes frequency ($\omega_{as} = 2\omega_{pump} - \omega_s$). The strength

of the measured signal changed with temporal overlap of the pump and stokes pulse, and with resonant position of the pump. The intensity of the measured coherent anti-Stokes signal also changed with orientation of carbon nanotube axis, relative to the polarization of the pump, showing a $cos^6\phi$ dependence, shown in Figure 4.7, which could lend some insight into the nonzero tensor elements of $\chi^{(3)}$. Another experimental study, done on four wave mixing, by Lui, suggests that there are other nonzero $\chi(3)$ tensor elements that contribute to the overall $\chi(3)$ [32].

There have not been any studies that experimentally measure the absolute value of $\chi^{(2)}$ for carbon nanotubes via third harmonic generation. No groups have experimentally investigated the relevant $\chi^{(2)}$ tensor elements that contribute to the overall $\chi^{(2)}$ signal.

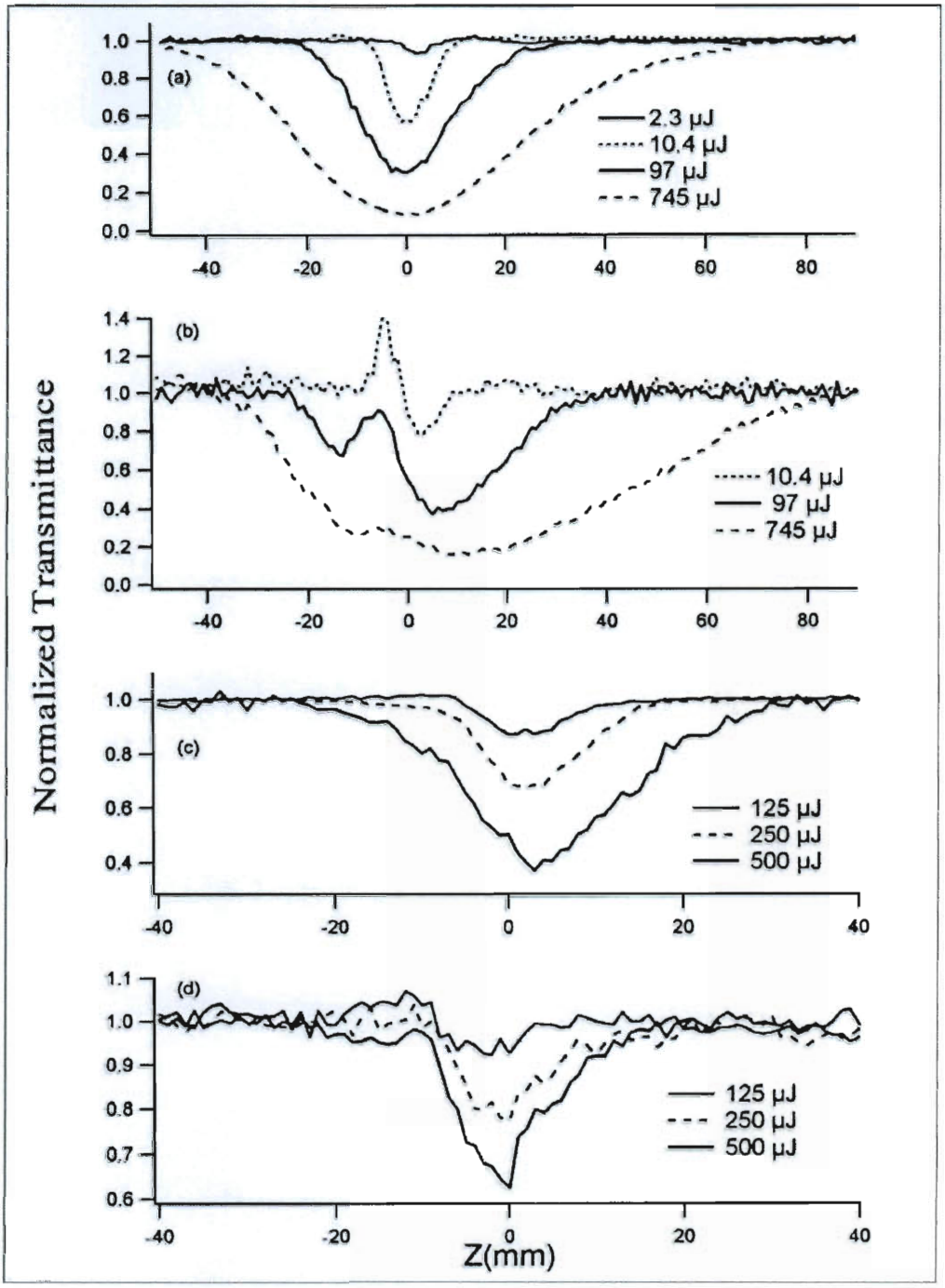

Figure 4.6 : Z scan measurements at different input energies for (a) 532 nm, large aperture; (b) 532 nm, small aperture; (c) 1064 nm, large aperture; and (d) 1064 nm, small aperture [26].

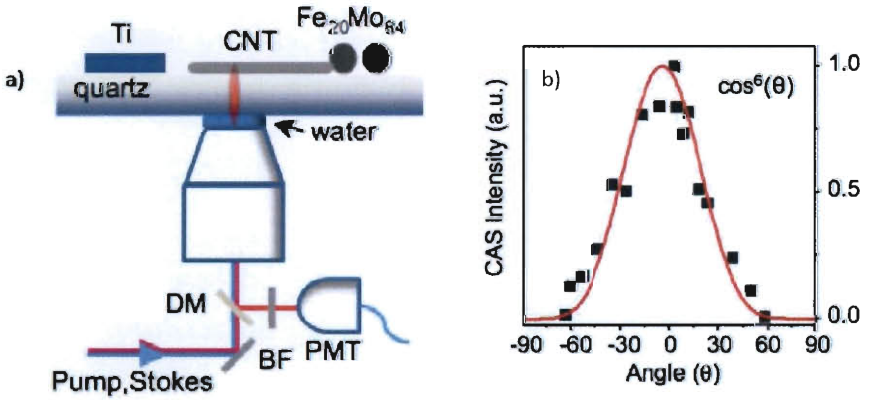

Figure 4.7 : (a) Schematic of fourwave mixing experiment; (b) Orientation dependence of the coherent anti-stokes signal [31].

Chapter 5

Experimental Procedure

5.1 Highly aligned SWNT sample preparation and characterization

There are many types of carbon nanotube samples that are used for optical experiments. Researchers have used solutions, films, as well as individual nanotubes for measurements, all of which have their advantages and disadvantages. In this work, we use highly aligned SWNT films on a variety of substrates. The highly aligned carbon nanotube carpets are grown via placing a catalyst lined substrate in a chemical vapor deposition reactor. The lines of catalysts are separated by a distance of 50 μm, and the self supporting carbon nanotubes are grown vertically to a height specified by growth time, as shown in Figure 5.1. The vertically aligned carpet is then separated from the catalyst substrate via a wet or dry etching process, to break the Fe-C bonds. Once the SWNTs have been lifted, they easily adhere to any substrate surface, creating a horizontally aligned film of SWNTs with little to zero overlap, depending on the initial growth height, as shown in Figure 5.1. The samples are highly aligned, as shown in Figure 5.2, where the highly aligned nanotube film acts as a perfect polarizer for terahertz light.

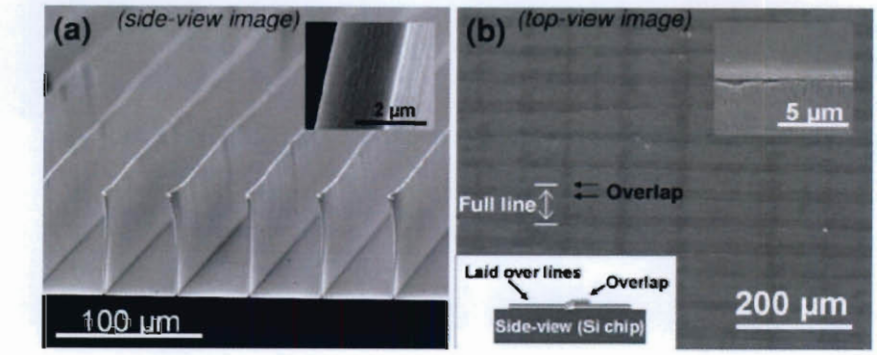

Figure 5.1 : (a) SEM image of vertically aligned SWNT carpets; (b) SEM image of horizontally aligned SWNT film after transfer to substrate. Sample shows minimal overlap [33].

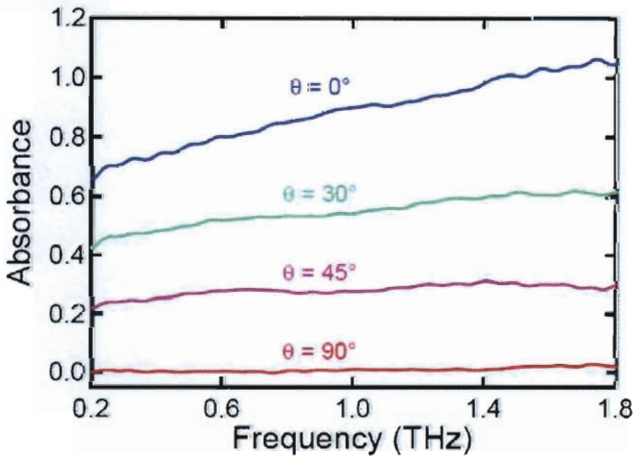

Figure 5.2 : (a) Terahertz absorption anisotropy for highly aligned SWNT film on sapphire [34].

5.2 Experimental setup for harmonic generation

5.2.1 Overview

In these experiments harmonic generation in samples with highly aligned SWNTs was measured. The harmonic signal was spectally resolved, and the orientation de-

pendence of this harmonic signal was also measured, relative to a linearly polarized fundamental. A schematic of the experimental setup is shown in figure (5.3). Ultra-intense mid-infrared light pulses, from an optically-pumped nonlinear laser, served fundamental source. This mid-infrared light passes through a series of long pass filters to remove any access light from the OPA. Most of the light passes through a beamsplitter and is incident on the sample, while the small reflected fraction served as a reference. The harmonic signal, generated in the sample, passes through a series of bk7 windows, to filter out the fundamental, and into an infrared detector . The sample is mounted on a rotational mount for orientation dependent measurements.

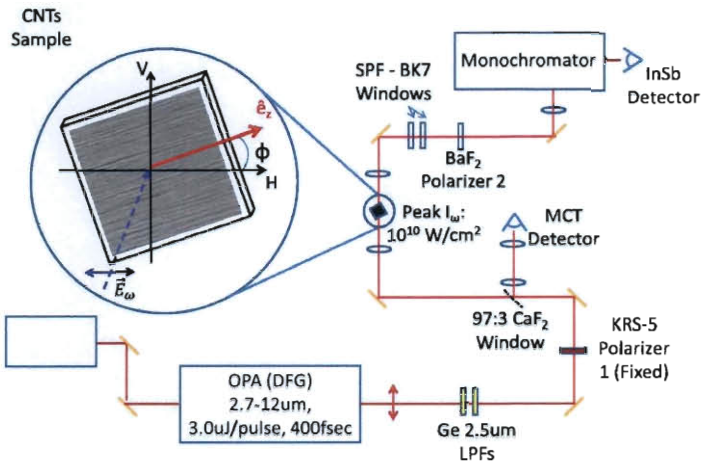

Figure 5.3 : Experimental setup for harmonic generation.

5.2.2 Chirped Pulse Amplifier and Optical Parametric Amplifier

Light at the fundamental frequency was produced from a Quantronix Optical Parametric Amplifier, which was pumped by a Clark-MXR Chirped Pulse Amplifier (CPA). In the CPA, a low intensity, short diode seed laser pulse was stretched

(chirped) using a grating, sent through an optically pumped gain medium (Ti-Sapphire), and compressed using a grating, to create ultra-intense (1 mJ/pulse), ultra short (200 fsec) pulses at a 1 kHz repetition rate. The OPA uses a nonlinear crystal, to create two pulses (signal and idler) whose sum total photon energy is equal to the energy of the pump. In this process, called optical parametric generation, the signal and idler wavelengths are tunable over a range from 1.2 to 2.7 μm. The signal and idler pulses are then propagated through a selection of nonlinear mixer crystals, which make the OPA source widely tunable over $0.3\mu m$ to $20\mu m$, with pulse energies ranging from 1 μJ/pulse to 100 μJ/pulse, and pulse width of $\sim$400 fsec.

5.2.3 Detectors

To measure the intesity of the generated harmonic signal, a liquid nitrogen cooled InSb detector was used, whose optimal detectivity range is from 1.5 to 2.8 μm. To measure the intensity of the fundamental, a liquid nitrogen cooled mercury cadmium telluride detector was used, whose optimum detectivity range is from 1.5 to 12 μm. These photovolactic detectors come equiped with a preamplifier for converting the detector output current to voltage, to be used by the box-car integrator and lock-in amplifier, making them ideal for measuring weak harmonic signals. They work optimally at 77K and have a response time of $\sim$1 μsec.

5.2.4 Filters

Germanium long pass filters were used to filter out any of the signal, idler, or pump pulses that could be senstive to the InSb detector, and pass the fundamental for harmonic generation at the sample position. After harmonic generation, BK7 windows were used as a short pass filter to pass the generated signal, and to ensure that no nonliear absorption from the fundamental occurs in the detector.

5.2.5 Beamsplitter and ratioing using a reference beam

The fluctuations from the nonlinear laser sources were monitored using a reference line, using a 0.1 mm thick CaF_2 window. The CaF_2 window allowed for 97% of the fundamental to be passed to the sample. For the second harmonic experiment, SHG from a reference GaAs substrate was used to correct for any pulse to pulse fluctuations in the SHG signal. For the third harmonic generation (THG) experiment, no reference crystal was used, because the reference input intensity was not large enough to generate THG, thus the pulse to pulse fluctuations in the third harmonic signal were corrected using cubed intensity of the reference, I_{ref}^3.

5.2.6 Lock-in amplifier and box-car integrator

Both the harmonic and reference signals were measured using a lock-in amplifier and box-car integrator. The lock-in amplifier takes the input signal and multiplies it by the reference signal (TTL signal from CPA), both of the same frequency and integrated over a time longer than the frequency, delivering an averaged DC signal (slowly varying AC signal). Any component (noise) that is not of the same frequency as the signal has an average value of zero, allowing for an excellent signal to noise ratio, when usign a lock-in. The lock-in was used to find the harmonic signal. A box car accepts a signal from a detector and integrates the signal under a predefined gate, or boxcar. Thus, any unwanted signal (noise) that is of the same frequency can be ignored by setting the box-car width such that it does not include the the unwanted signal. The box-car integrator allows data to be collected on the frequency timescale of the input signal, making pulse to pulse measurements possible. The data presented in the following studies were collected using the box-car integrator.

5.2.7 Rotational sample mount for orientation dependent measurements

The sample was placed on two rotational mounts for the second harmonic generation experiment. The sample was rotated through an angle θ to induce SHG from the GaAs substrate (centrosymmetric at normal incidence). The axis of rotation was chosen such that one component of the incident fundamental remained in the plane of the GaAs substrate, which we called the TE axis. The axis perpendicular to this mode and the direction of propagation $\vec{k}$, we called the TM axis, as shown in Figure 5.4. The sample was then rotated through an angle ϕ, starting from a position where a TE polarized fundamental is parallel to the SWNT axis, to examine the polarization dependence of the second harmonic from the sample, which can be seen in Figure 5.5.

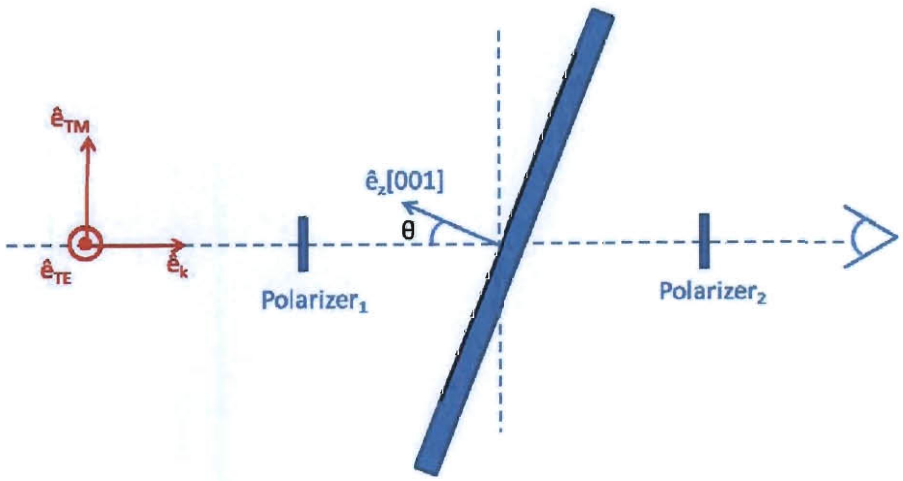

Figure 5.4 : Side view of the polarized fundamental incident on the sample, for second harmonic generation from highly aligned SWNTs on GaAs

The sample was placed on one rotational mount for the THG experiment. Data was taken at normal incidence, as we rotate through an angle, ϕ, starting from a position where the horizontally polarized fundamental is parallel to the SWNT axis.

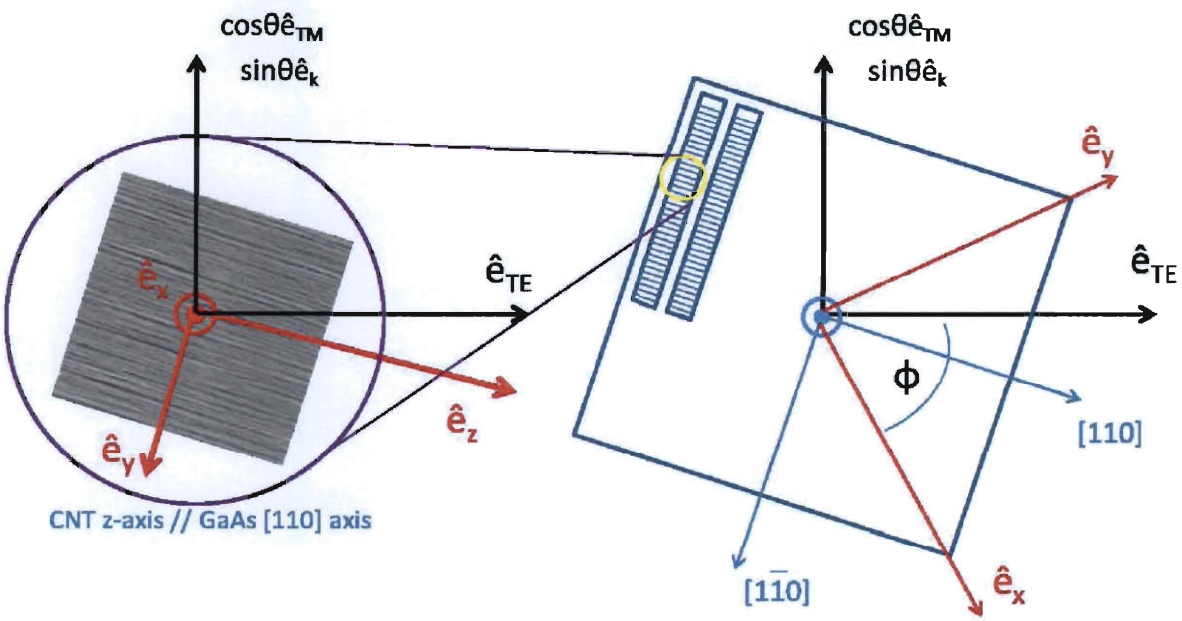

Figure 5.5 : In-substrate-plane view of the polarized fundamental incident on the sample, for second harmonic generation from highly aligned SWNTs on GaAs. Projections of the TM and $\vec{k}$ propagation components are shown here.

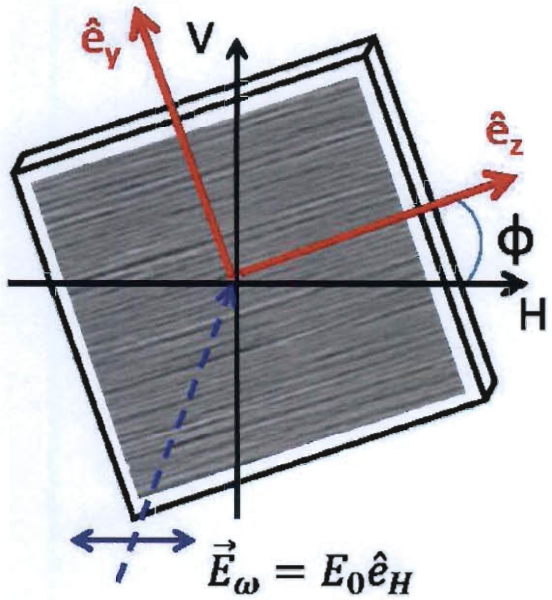

Figure 5.6 : Normal incidence view for of a horizontally polarized fundamental incident on the sample, for third harmonic generation from highly aligned SWNTs on sapphire.

Chapter 6

Second Harmonic Generation from Highly Aligned Single-Walled Carbon Nanotubes

6.1 Experimental results

Orientation (ϕ) dependence of the second harmonic generated from a sample containing highly aligned SWNTs on GaAs and from its reference, GaAs was studied. Figure 6.1 shows data for a second harmonic produced from TE polarized fundamental, and the SHG produced is polarized in the TE and TM directions, while Figure 6.2 shows data collected for a TM polarized fundamental. The same measurements were taken for the GaAs refernce, and are plotted in Figures 6.3 and 6.4.

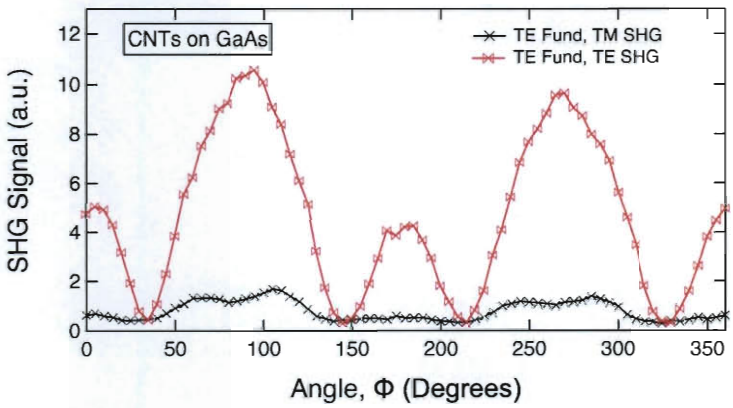

Figure 6.1 : ϕ dependence of the second harmonic signal, generated from the SWNT film on GaAs, for a TE polarized fundamental. See Figure 5.5 for the definition of ϕ. $\phi = 0$ corresponds to light polarization parallel to the nanotube axis (GaAs cleaved axis).

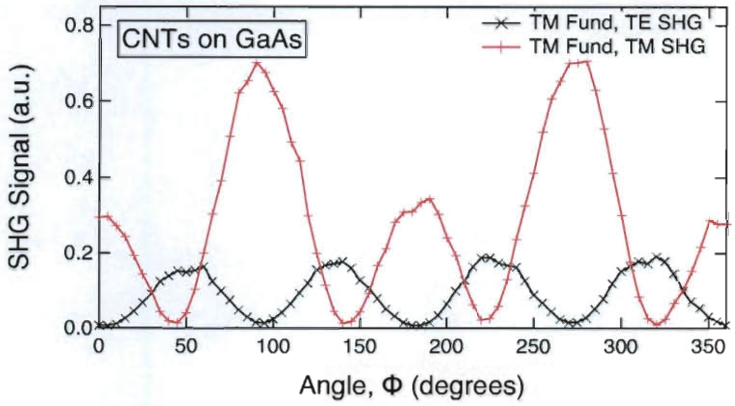

Figure 6.2 : ϕ dependence of the second harmonic signal, generated from the SWNT film on GaAs, for a TM polarized fundamental. See Figure 5.5 for the definition of ϕ. $\phi = 0$ corresponds to light polarization parallel to the nanotube axis (GaAs cleaved axis).

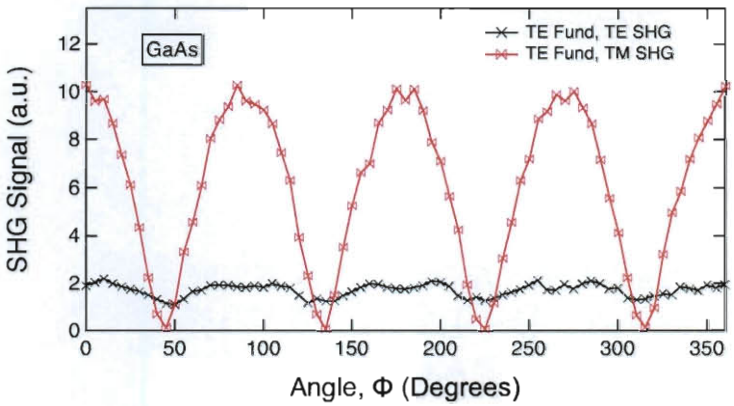

Figure 6.3 : ϕ dependence of the second harmonic signal, generated from the GaAs substrate, for a TE polarized fundamental. See Figure 5.5 for the definition of ϕ. $\phi = 0$ corresponds to light polarization parallel to the nanotube axis (GaAs cleaved axis).

From these figures, there are some notable features to be discussed. There are anisotropies in the SHG signal, shown in Figure 6.1. When the light is polarized

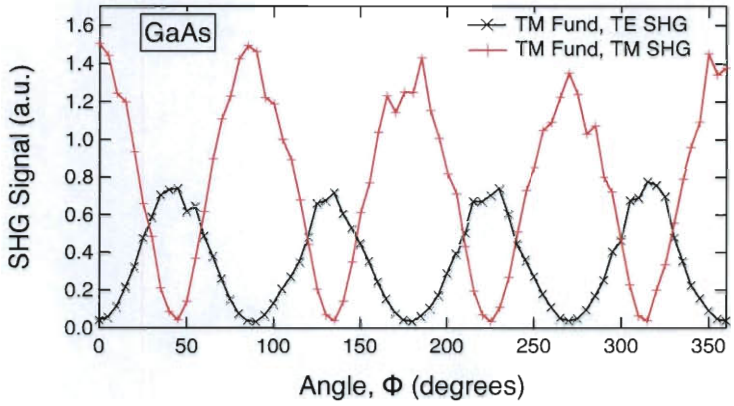

Figure 6.4 : ϕ dependence of the second harmonic signal, generated from the GaAs substrate, for a TM polarized fundamental. See Figure 5.5 for the definition of ϕ. $\phi = 0$ corresponds to light polarization parallel to the nanotube axis (GaAs cleaved axis).

parallel ($\phi = 0$) to the carbon nanotube axis, the generated second harmonic signal is lower than that of the case where the fundamental is perpendicular ($\phi = 90$) to the nanotubes. Comparing the sample versus the reference for a TE polarized fundamental and a TM polarized SHG, we see that there is a shift in the minimum from 45 degrees in the GaAs reference to 30 degrees in the sample. This minimum is also finite in the sample, as compared to zero in the GaAs case.

6.2 Data analysis

The individual contributions from the GaAs and SWNT film can be calculated, considering the i-th component of the induced second harmonic field from an undepleted pump moving through crystal length, l, written as

$$E_{2\omega,i} = \frac{i\omega l}{n_{2\omega}c\xi}\left[\sum_{j,k}\frac{1}{2}\chi^{(2)}_{ijk}E_{\omega,j}E_{\omega,k}\right]\sin\xi e^{i\xi} \equiv A_{\mathrm{GaAs}}\left[\sum_{j,k}\frac{1}{2}\chi^{(2)}_{ijk}E_{\omega,j}E_{\omega,k}\right], \quad (6.1)$$

where ξ is a phase shift parameter, and the factor in brackets in the nonlinear polarization at the second harmonics from Equation (3.3). From this equation, it can be shown (calculations are provided in A) that the GaAs contributions to the overall SHG signal for TE/TM polarized fundamental and TE/TM polarized SHG, considering its crystal symmetries, are:

$$E_{2\omega,TE} = B_{\mathrm{GaAs}}(\theta)A_{\mathrm{GaAs}}\chi^{(2)}_{\mathrm{GaAs}}I_{\omega,TE}\cdot 0 = 0 \quad (6.2)$$

$$E_{2\omega,TM} = B_{\mathrm{GaAs}}(\theta)A_{\mathrm{GaAs}}\chi^{(2)}_{\mathrm{GaAs}}I_{\omega,TE}\cos 2\phi \quad (6.3)$$

$$E_{2\omega,TE} = B_{\mathrm{GaAs}}(\theta)A_{\mathrm{GaAs}}\chi^{(2)}_{\mathrm{GaAs}}I_{\omega,TM}\sin 2\phi \quad (6.4)$$

$$E_{2\omega,TM} = B_{\mathrm{GaAs}}(\theta)A_{\mathrm{GaAs}}\chi^{(2)}_{\mathrm{GaAs}}I_{\omega,TM}\cos 2\phi. \quad (6.5)$$

These calculations are consistent with the ϕ dependence of the SHG intensity ($I_{2\omega} = E^2_{2\omega}$) data collected for the reference GaAs substrate, as seen in Figure 6.5.

The highly aligned SWNT contributions to the overall SHG signal are:

$$E_{2\omega,TE} = B_{\mathrm{CNT}}(\theta)A_{\mathrm{CNT}}\chi^{(2)}_{\mathrm{CNT}}I_{\omega,TE}\cdot 0 = 0 \quad (6.6)$$

$$E_{2\omega,TM} = B_{\mathrm{CNT}}(\theta)A_{\mathrm{CNT}}\chi^{(2)}_{\mathrm{CNT}}I_{\omega,TE}\sin 2\phi \quad (6.7)$$

$$E_{2\omega,TE} = B_{\mathrm{CNT}}(\theta)A_{\mathrm{CNT}}\chi^{(2)}_{\mathrm{CNT}}I_{\omega,TM}\sin^2\phi \quad (6.8)$$

$$E_{2\omega,TM} = B_{\mathrm{CNT}}(\theta)A_{\mathrm{CNT}}\chi^{(2)}_{\mathrm{CNT}}I_{\omega,TM}(-\cos\theta\sin 2\phi + \cos\theta\sin 2\phi) = 0. \quad (6.9)$$

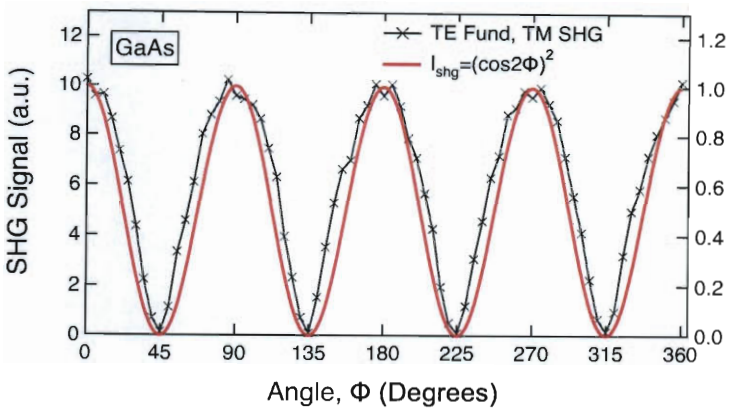

Figure 6.5 : For a TE polarized fundamental, and TM polarized SHG, the GaAs substrate shows excellent agreement between measured ϕ dependence and calculated ϕ dependence. $\phi = 0$ corresponds to light polarization parallel to the nanotube axis (GaAs cleaved axis).

These calculations for the nanotube contribution must be combined with the GaAs contribution, because the nanotubes are aligned on a GaAs substrate. Simulations for the combined contribution considering a coherent contribution $I_{2\omega,coh} = (E_{2\omega,GaAs} + \epsilon E_{2\omega,CNT})^2$ and incoherent contribution $I_{2\omega,incoh} = E^2_{2\omega,GaAs} + \epsilon E^2_{2\omega,CNT}$, are shown in Figures 6.6 and 6.7, respectively (ϵ: relative contribution from CNTs). The features in Figures 6.6 and 6.7 the do not match the features in the experimentally measured data in Figure 6.2, thus there is no coherent nor incoherent contribution to this measured SHG signal.

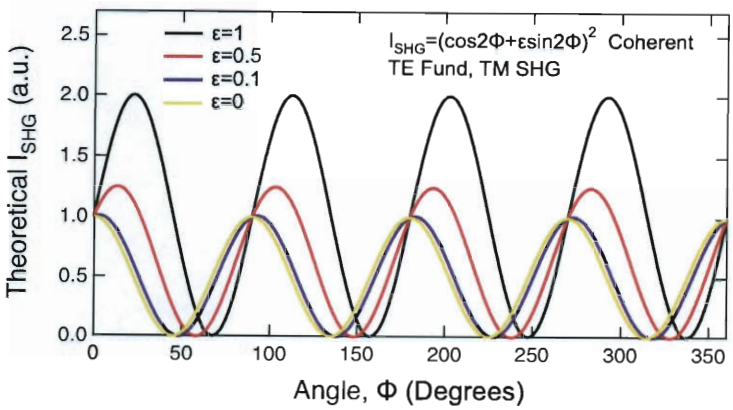

Figure 6.6 : For a TE polarized fundamental, and TM polarized SHG, the coherent contribution from the GaAs substrate and the highly aligned CNTs is shown. We varied the relative contribution ϵ from the CNTs. $\phi = 0$ corresponds to light polarization parallel to the nanotube axis (GaAs cleaved axis).

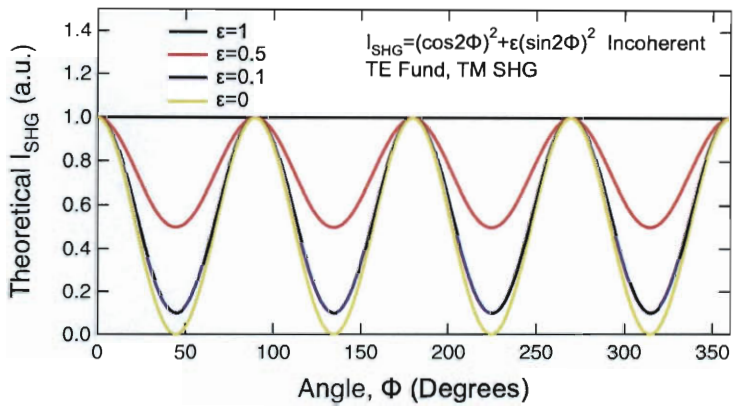

Figure 6.7 : For a TE polarized fundamental, and TM polarized SHG, the incoherent contribution from the GaAs substrate and the highly aligned CNTs is shown. We varied the relative contribution ϵ from the CNTs. $\phi = 0$ corresponds to light polarization parallel to the nanotube axis (GaAs cleaved axis).

We **measured the transm**ission anisotropy through the CNTs using Fourier Transform Infrared Spectroscopy (FTIR), shown in Figure 6.8.

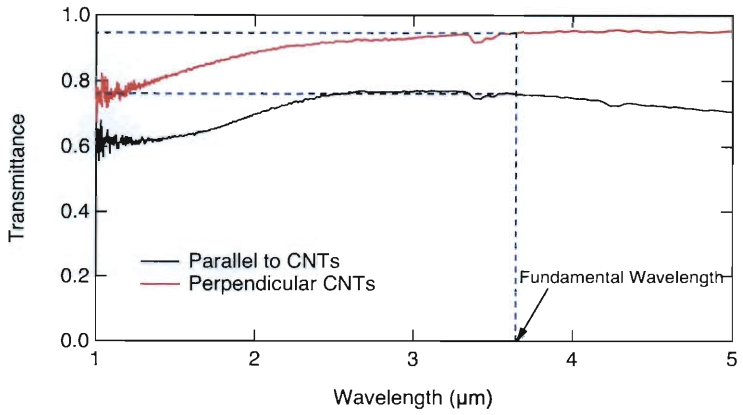

Figure 6.8 : FTIR data, illustrating the anisotropic transmission shown for light polarized parallel and perpendicular to the highly aligned SWNT film.

Thus, we considered the GaAs contributions to the SHG signal assuming that the fundamental undergoes anisotropic absorption from the highly aligned SWNT film. The relationships are as follows:

$$E_{2\omega,TE} = B_{\mathrm{GaAs}}(\theta) A_{\mathrm{GaAs}} \chi^{(2)}_{\mathrm{GaAs}} I_{\omega,TE} \cdot 0 = 0 \tag{6.10}$$

$$E_{2\omega,TM} = B_{\mathrm{GaAs}}(\theta) A_{\mathrm{GaAs}} \chi^{(2)}_{\mathrm{GaAs}} I_{\omega,TE} \left[(\%T_{\parallel}) \cos^2\phi - (\%T_{\perp}) \sin^2\phi \right] \tag{6.11}$$

$$E_{2\omega,TE} = B_{\mathrm{GaAs}}(\theta) A_{\mathrm{GaAs}} \chi^{(2)}_{\mathrm{GaAs}} I_{\omega,TM} (\sqrt{\%T_{\parallel}} - \sqrt{\%T_{\perp}}) \sin 2\phi \tag{6.12}$$

$$E_{2\omega,TM} = B_{\mathrm{GaAs}}(\theta) A_{\mathrm{GaAs}} \chi^{(2)}_{\mathrm{GaAs}} I_{\omega,TM} \left[\begin{array}{c} 2\sqrt{\%T_{\perp}} + \%T_{\perp} - 2\sqrt{\%T_{\parallel}} - \%T_{\parallel} \\ +(2\sqrt{\%T_{\perp}} + \%T_{\perp} + 2\sqrt{\%T_{\parallel}} + \%T_{\parallel}) \cos 2\phi \end{array} \right]. \tag{6.13}$$

Simulations for these relationships are shown in Figures 6.9, 6.10, and 6.11. Using the values measured for $\%T_{\parallel}$ and $\%T_{\perp}$, we can see that the theoretically calculated spectum is in good agreement with the spectra measured experimentally, as shown in Figure 6.12.

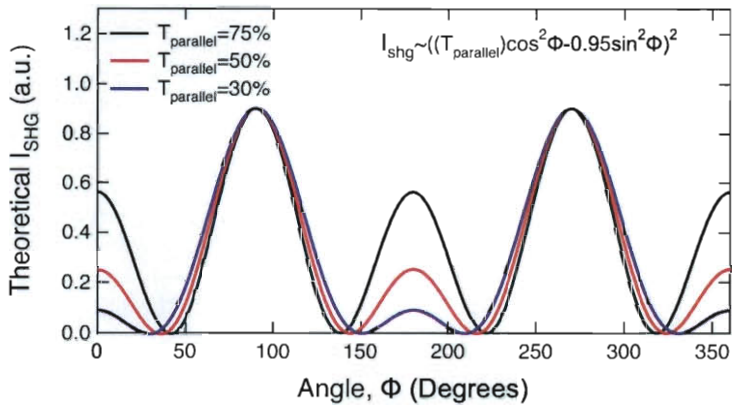

Figure 6.9 : Simulations for a TE polarized fundamental, and TM polarized SHG, assuming the fundamental undergoes an anisotropic transmission $T_{\|}$ and $T_{\perp}$ from the carbon nanotubes, and the second is generated from only the GaAs substrate. The following simulation shows ϕ dependence for a fixed $T_{\perp} = 95\%$ and variable $T_{\|}$. $\phi = 0$ corresponds to light polarization parallel to the nanotube axis (GaAs cleaved axis).

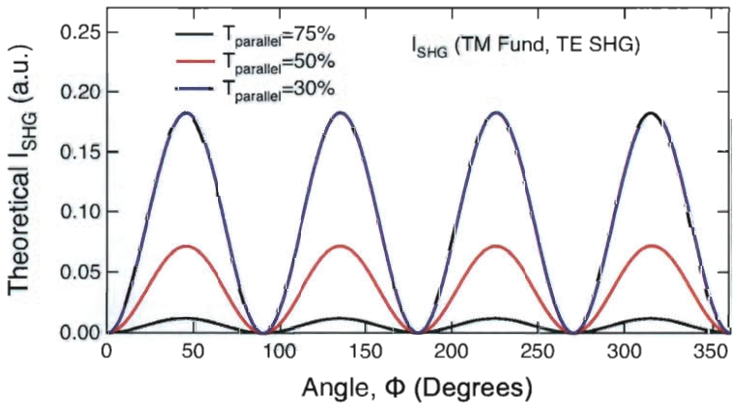

Figure 6.10 : Simulations for a TM polarized fundamental, and TE polarized SHG, assiming the fundamental undergoes an anisotropic transmission $T_{\|}$ and $T_{\perp}$ from the carbon nanotubes, and the second is generated from only the GaAs substrate. The following simulation shows ϕ dependence for a fixed $T_{\perp} = 95\%$ and variable $T_{\|}$. $\phi = 0$ corresponds to light polarization parallel to the nanotube axis (GaAs cleaved axis).

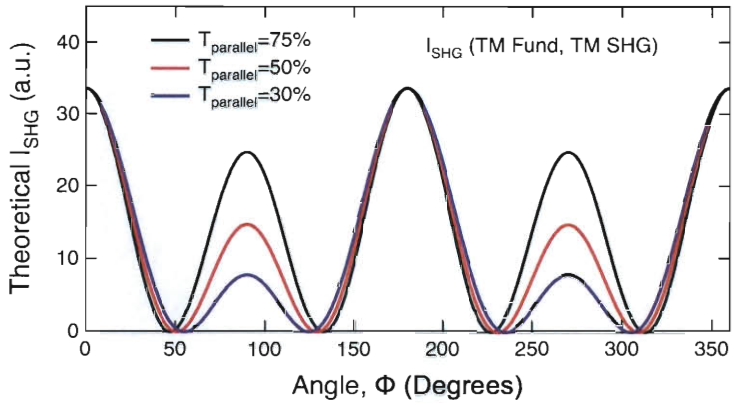

Figure 6.11 : Simulations for a TM polarized fundamental, and TM polarized SHG, assuming the fundamental undergoes an anisotropic transmission $T_{\|}$ and $T_{\perp}$ from the carbon nanotubes, and the second is generated from only the GaAs substrate. The following simulation shows ϕ dependence for a fixed $T_{\perp} = 95\%$ and variable $T_{\|}$. $\phi = 0$ corresponds to light polarization parallel to the nanotube axis (GaAs cleaved axis).

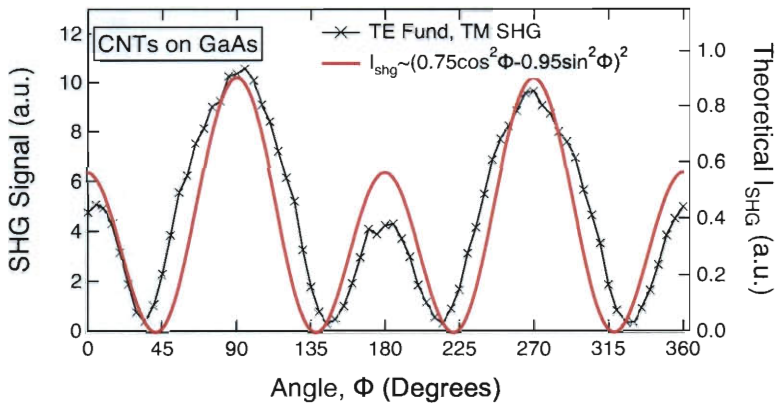

Figure 6.12 : Experimentally measured and theoretically calculated TM polarized SHG for a TE polarized fundamental assuming the fundamental undergoes an anisotropic transmission $T_{\|} = 0.75$ and $T_{\perp} = 0.95$ from the carbon nanotubes. $\phi = 0$ corresponds to light polarization parallel to the nanotube axis (GaAs cleaved axis).

6.3 Discussion and conclusion

From the calculations presented in the Section ??, we see that the second harmonic signal measured from the sample was generated by the GaAs substrate. The shift in the minimum and anisotropic features in the SHG signal can be attibuted to an anisotropic absoption from the highly aligned SWNT film. There are a few explinations for the lack of SHG signal measured from the nanotubes. The thin SWNT film is made of large diameter nanotubes of unknown chirality. The sample contains left handed and right handed chirality tubes, thus the induced second harmonic effect in right handed CNTs can be canceled by left hand chirality tubes. Because the chirality of the SWNTs are not known, we do not know whether we are on resonance with E_{11} or E_{22} energy transitions, which has been shown to increase $\chi^{(2)}$. According to Guo, the magnitude of the absolute value of the second order susceptibility gets smaller as the diameter of the nanotubes gets larger ($\chi^{(2)}_{\text{graphene}} = 0$), thus by having larger diameter tubes, the signal is expected to be smaller. Also, because we are using a SWNT film, the interaction length with the single layer of SWNTs is small, compared to that of GaAs.

There are still some unclear features of the ϕ dependent second harmonic signal. The ratio of the anisotropic absorption did not explain the full shift of the minimum seen in the signal. The minimum also has a finite value in the measurements made with the SWNT sample. In future experiments, we want to minimize the second harmonic signal produced in the from the sample substrate, so that any signal seen could be attributed to the SWNT film. Also, we want to look at right-handed and left-handed nanotubes seperately.

Chapter 7

Third Harmonic Generation from Highly Aligned Single Walled Carbon Nanotubes

7.1 Experimental results

In order to ensure that the only produced harmonic was indeed coming from the SWNT film, a substrate with relatively low $\chi^{(2)}$ and $\chi^{(3)}$ is needed. Thus, measurements from a sample of highly aligned SWNTs on sapphire was used. Figure 7.1 shows a spectrally resolved third harmonic signal and its fundamental generated from our SWNT sample. Changing the fundamental input wavelength caused a subsequent shift in the third harmonic signal, as shown in Figure 7.2. Figure 7.3 shows third harmonic generation from the sapphire reference, versus what was measured with the SWNT sample. Figure 7.4 shows the same third harmonic signal for a fundamental polarized parallel to carbon nanotube axis, versus perpendicular to the nanotube axis.

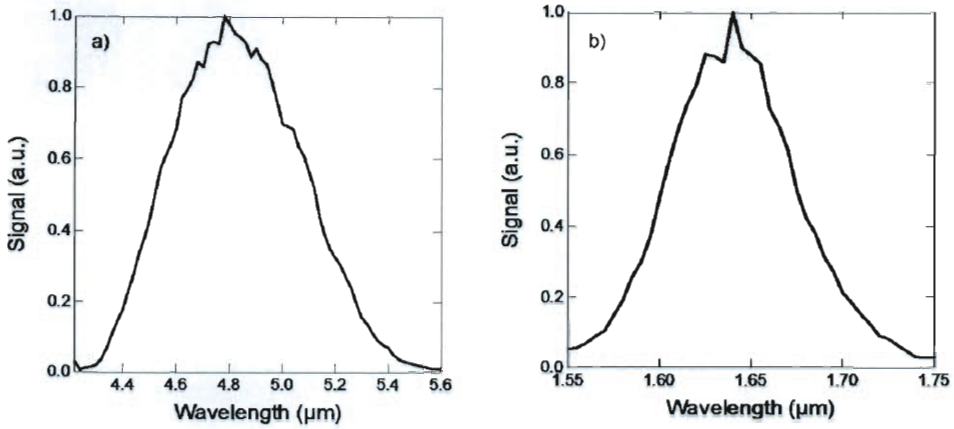

Figure 7.1 : (a) Generated third harmonic from highly aligned SWNTs on sapphire and (b) its fundamental. The SWNTs are aligned parallel to the incident fundamental and the induced THG is polarized parallel to the fundamental.

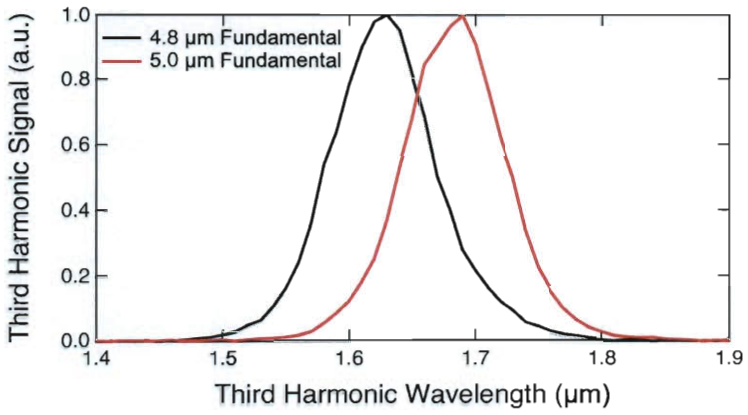

Figure 7.2 : Shift in third harmnic signal due to a shift in the fundamental from 4.8 to 5.0 μm. The SWNTs are aligned parallel to the incident fundamental and the induced THG is polarized parallel to the fundamental.

This data indicates that a third harmonic signal is being produced from the SWNT film. Thus, orientation (ϕ) dependence was also taken, and can be seen in Figures 7.5 and 7.6. Here, the third harmonic signal is polarized parallel and perpendicular

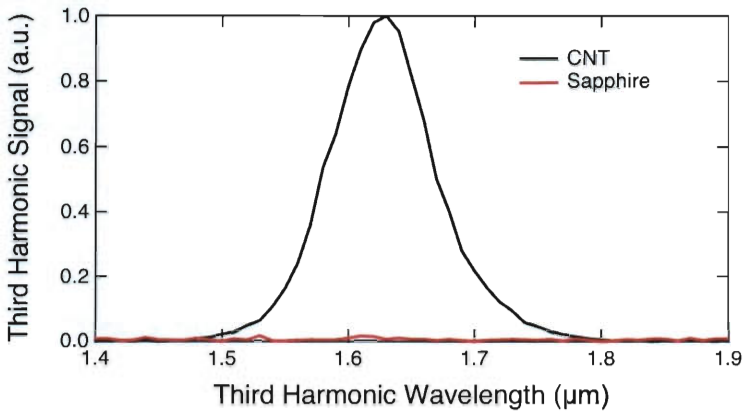

Figure 7.3 : Produced third harmonic signal from SWNT film on sapphire substrate, versus the signal generated from sapphire substrate. The SWNTs are aligned parallel to the incident fundamental and the induced THG is polarized parallel to the fundamental.

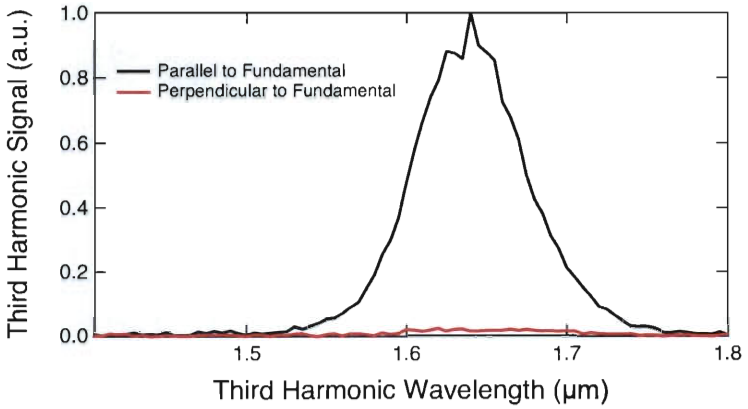

Figure 7.4 : Generated third harmonic from highly aligned SWNTs aligned parallel versus perpendicular to the fundamental. The induced THG is polarized parallel to the fundamental.

to the incident fundamental polarization.

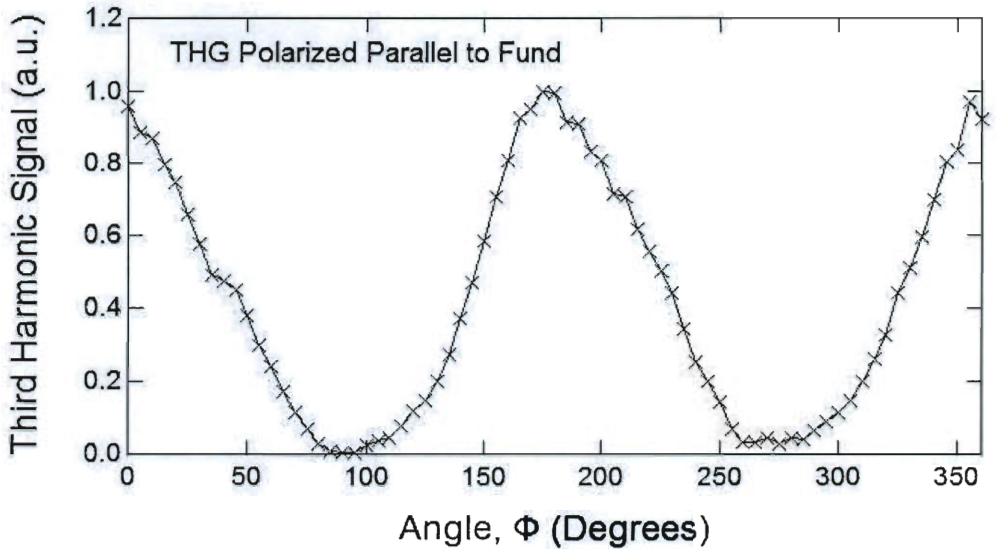

Figure 7.5 : ϕ dependence of the third harmonic signal, generated from the SWNT film on Sapphire. The third harmonic signal is polarized parallel to the fundamental. $\phi = 0$ corresponds to light polarization parallel to the nanotube axis.

From these figures, there are some notable features to be discussed. There are anisotropies in the THG signal, shown in Figure 7.4. When the light is polarized parallel to the carbon nanotube axis, the generated third harmonic signal is almost 2 orders of magnitude larger than that of the case where the fundamental is perpendicular to the nanotubes. This information could give us some insight into the relevant nonzero $\chi^{(3)}$ tensor elements.

7.2 Data analysis

The orientation dependence of the SWNT film can be explored by considering the i-th component of the induced third harmonic field,

$$E_{3\omega,i} = A_{\mathrm{CNT}} \left[\sum_{j,k,l} \chi^{(3)}_{ijkl} E_{\omega,j} E_{\omega,k} E_{\omega,l} \right], \tag{7.1}$$

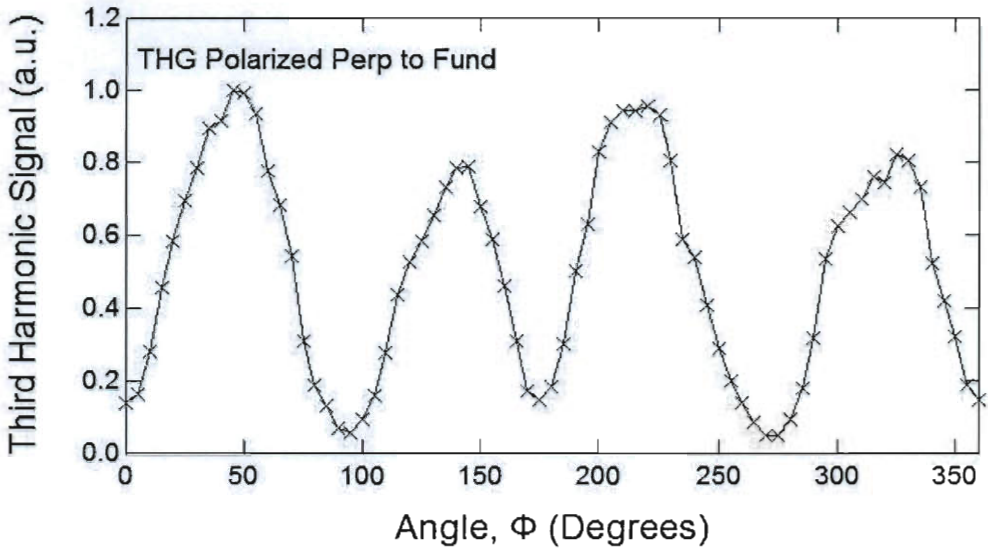

Figure 7.6 : ϕ dependence of the third harmonic signal, generated from the SWNT film on Sapphire. The third harmonic signal is polarized perpendicular to the fundamental. $\phi = 0$ corresponds to light polarization parallel to the nanotube axis.

where A_{CNT} is a constant containing information about the fundamental-third harmonic interaction, and a phase shift parameter, and the factor in brackets in the nonlinear polarization at the third harmonic from Equation 3.4. From this equation, it can be shown (similar to the calculations provided in A) that the orientation dependence of a third harmonic signal generated from carbon nanotubes, considering $\chi^{(3)}_{zzzz}$ is the only relevant tensor component, is represented by the following relationships

$$E_{3\omega,\parallel} = A_{\mathrm{CNT}} \chi^{(3)}_{\mathrm{CNT}} I_{\omega} \cos^4 \phi \tag{7.2}$$

and

$$E_{3\omega,\perp} = A_{\mathrm{CNT}} \chi^{(3)}_{\mathrm{CNT}} I_{\omega} \cos^3 \phi \sin \phi \tag{7.3}$$

These calculations, however, were not consistent with the ϕ dependence of the THG intensity ($I_{3\omega} = E^2_{3\omega}$) data collected for the highly aligned SWNT film as shown in

Figures 7.7 and 7.8.

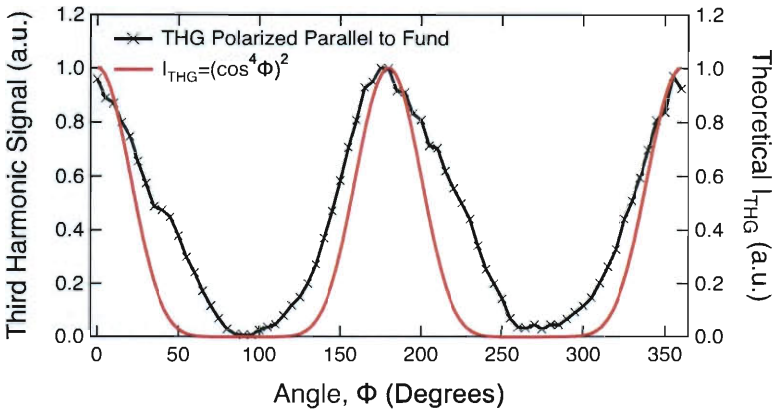

Figure 7.7 : ϕ dependence of the measured third harmonic signal generated from the SWNT film on Sapphire with theoretical calculations assuming $\chi^{(3)}_{zzzz}$ is the dominant $\chi^{(3)}$ tensor element. The third harmonic signal is polarized parallel to the fundamental. $\phi = 0$ corresponds to light polarization parallel to the nanotube axis.

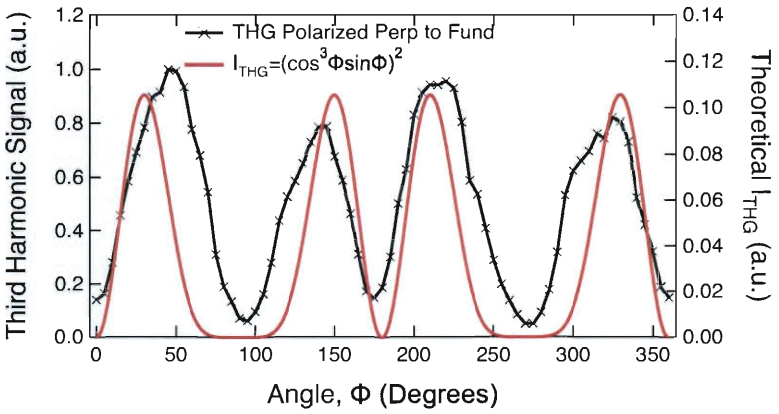

Figure 7.8 : ϕ dependence of the measured third harmonic signal generated from the SWNT film on Sapphire with theoretical calculations assuming $\chi^{(3)}_{zzzz}$ is the dominant $\chi^{(3)}$ tensor element. The third harmonic signal is polarized perpendicular to the fundamental. $\phi = 0$ corresponds to light polarization parallel to the nanotube axis.

In order to further explore the relevant $\chi^{(3)}$ tensor elements, we will consider $\chi^{(3)}_{zzzz}$ to be the dominant component, but also consider $\chi^{(3)}_{zzxx}$, $\chi^{(3)}_{zxxz}$, $\chi^{(3)}_{zxzx}$, $\chi^{(3)}_{zzyy}$, $\chi^{(3)}_{zyyz}$, and $\chi^{(3)}_{zyzy}$ to be relevant nonzero tensor elements, as suggested by the four wave mixing experiment, executed by Lui et al. [[32]]. If we take the ratio of the absolute value of the relevant tensor elements to be

$$\chi^{(3)}_{zzzz} = \alpha\chi^{(3)}_{zzxx} = \alpha\chi^{(3)}_{zxxz} = \alpha\chi^{(3)}_{zxzx} = \alpha\chi^{(3)}_{zzyy} = \alpha\chi^{(3)}_{zyyz} = \alpha\chi^{(3)}_{zyzy}, \tag{7.4}$$

then the orientation dependence of a third harmonic signal can be described by the equations below.

$$E_{3\omega,\parallel} = A_{\mathrm{CNT}}\chi^{(3)}_{\mathrm{CNT}}I_{\omega}(\cos^4\phi + 3\alpha\cos^2\phi\sin^2\phi) \tag{7.5}$$

and

$$E_{3\omega,\perp} = A_{\mathrm{CNT}}\chi^{(3)}_{\mathrm{CNT}}I_{\omega}(\cos^3\phi\sin\phi + 3\alpha\cos\phi\sin^3\phi) \tag{7.6}$$

Simulations for the ϕ dependence for the third harmonic signal based on these equations are shown in Figures 7.9 and 7.10. The measured THG spectrum are in excellent agreement with the theoretially calculated THG, as shown in Figures 7.11 and 7.12.

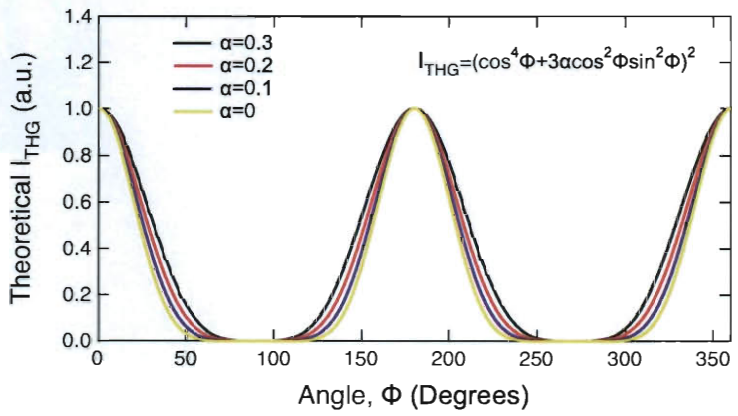

Figure 7.9 : Simulations for a THG signal polarized parallel to the fundamental, considering the $\chi^{(3)}$ tensor contribution realationship is $\chi^{(3)}_{zzzz} = \alpha\chi^{(3)}_{zzxx}$. The following simulation shows ϕ dependence for variable α. $\phi = 0$ corresponds to light polarization parallel to the nanotube axis.

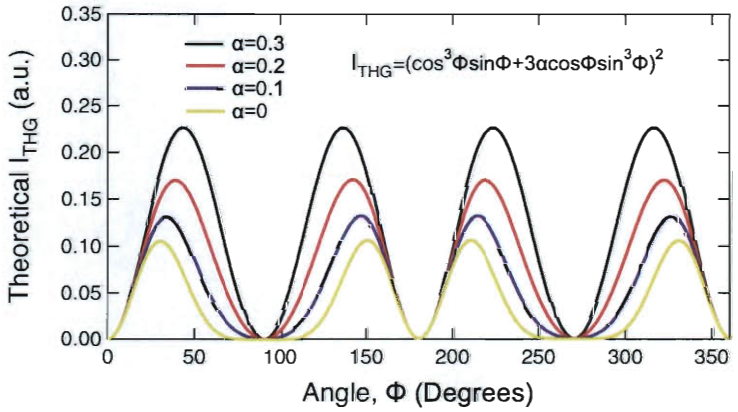

Figure 7.10 : Simulations for a THG signal polarized perpendicular to the fundamental, considering the $\chi^{(3)}$ tensor contribution realationship is $\chi^{(3)}_{zzzz} = \alpha\chi^{(3)}_{zzzz}$. The following simulation shows ϕ dependence for variable α. $\phi = 0$ corresponds to light polarization parallel to the nanotube axis.

7.3 Discussion and conclusion

From the calculations presented in the Section 7.2, it can be shown that the third harmonic signal measured from the higly aligned SWNT sample on sapphire had

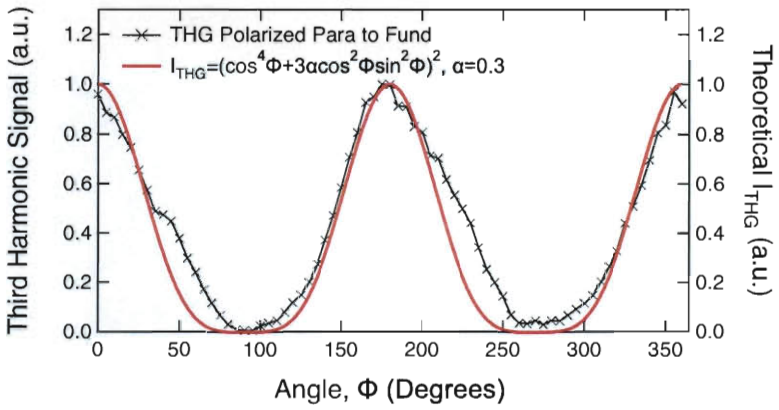

Figure 7.11 : Experimentally measured spectum with theoretically calculated spectrum for a THG signal polarized parallel to the fundamental, considering the $\chi^{(3)}$ tensor contribution realationship is $\chi^{(3)}_{zzzz} = \alpha\chi^{(3)}_{zzxx}$. The following simulation shows ϕ dependence for variable α. $\phi = 0$ corresponds to light polarization parallel to the nanotube axis.

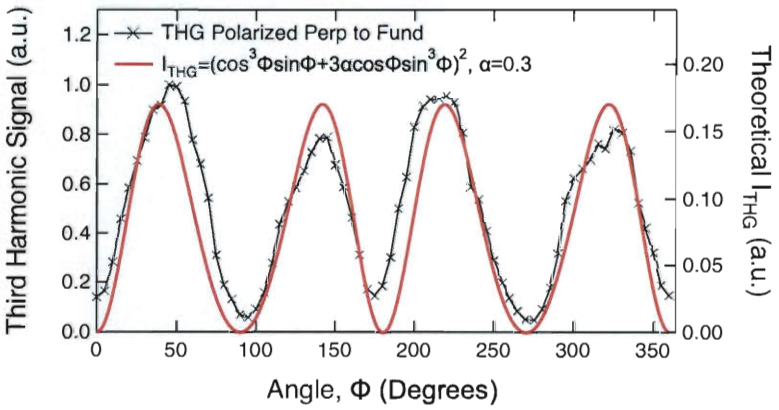

Figure 7.12 : Experimentally measured spectum with theoretically calculated spectrum for a THG signal polarized perpendicular to the fundamental, considering the $\chi^{(3)}$ tensor contribution realationship is $\chi^{(3)}_{zzzz} = \alpha\chi^{(3)}_{zzxx}$. The following simulation shows ϕ dependence for variable α. $\phi = 0$ corresponds to light polarization parallel to the nanotube axis.

contributions from weaker $\chi^{(3)}$ tensor elements. These weaker components are approximately 1/3 the strength of the dominant $\chi^{(3)}_{zzzz}$ component, and is in excellent agreement with Lui's experimental findings. In the future we would like to calculate the absolute value of $\chi^{(3)}_{THG}$ for carbon nanotubes.

Chapter 8

Summary

Through orientation dependent experiments we were able to the conclude that the cause of the anisotropic features in our second harmonic spectra from highly aligned SWNTs on GaAs were caused by an absoption anisotropy by the carbon nanotube film followed by second harmonic generation in the GaAs substrate. The calculations did not explain the presence of a finite minimum, which had been shifted by more than what had been calculated. Because the sample The lack of carbon nanotube contribution to the overall SHG signal could be explained by the presence of random chirality large diameter tubes in the sample. The zigzag and armchair tubes have inversion symmetry and the presence left-handed and right-handed chiral tubes introduce an inversion symmetry as well. This particular sample would be an ideal canditate for a mid-infrared photodetector, because of the unique electronic properties and its ability to absorb at long wavelengths.

By changing the substrate material for our harmonic generation experiment to sapphire, we were successfully able to measure third harmonic generation in highly aligned SWNTs. Through orientation dependent experiments, the relevant nonzero tensor elements for $\chi^{(3)}$ were extracted. We were also able to calculate the relative contribution of each tensor element to the nonlinear susceptibility. These experiments have opened doors to the possibility of other future experiments on the nonlinear properties of nanotubes, like measuring the absolute value of $\chi^{(3)}$, by comparing our measured intensity of the generated third harmonic signal to that of a material with

known $\chi^{(3)}$. If carbon nanotubes are found to have a large $\chi^{(3)}$, then it will be an ideal candidate for optical switching applications.

Appendices

Appendix A

Calculation of SHG ϕ Dependence from Highly Aligned Carbon Nanotubes on GaAs

A.1 Introduction

In order to consider the GaAs contribution to the SHG after the anisotropic absorption of the incident fundamental by the cabon nanotubes, we must refer to Figures 5.4 and 5.4. The three ortho-normal vectors $\hat{e}_{\mathrm{TM}}$, $\hat{e}_{\mathrm{TE}}$, and $\hat{e}_k$ must be projected onto the directions parallel and perpendicular to the carbon nanotube axes (parallel to the cleaved edges of GaAs). These vectors can be expressed as superpositions of the basis vectors $\hat{e}_{[1\bar{1}0]}$, $\hat{e}_{[110]}$, and $\hat{e}_{[001]}$ as

$$\hat{e}_{\mathrm{TM}} = -\cos\theta\cos\phi\hat{e}_{[1\bar{1}0]} - \cos\theta\sin\phi\hat{e}_{[110]} + \sin\theta\hat{e}_{[001]} \tag{A.1}$$

$$\hat{e}_{\mathrm{TE}} = -\sin\phi\hat{e}_{[1\bar{1}0]} + \cos\phi\hat{e}_{[110]} \tag{A.2}$$

$$\hat{e}_k = -\sin\theta\cos\phi\hat{e}_{[1\bar{1}0]} - \sin\theta\sin\phi\hat{e}_{[110]} - \cos\theta\hat{e}_{[001]}. \tag{A.3}$$

Thus, the two coordinate systems can be connected using rotation matrix $\tilde{R}(\theta,\phi)$ as

$$\begin{pmatrix} \hat{e}_{\mathrm{TM}} \\ \hat{e}_{\mathrm{TE}} \\ \hat{e}_k \end{pmatrix} = \tilde{R}(\theta,\phi) \begin{pmatrix} \hat{e}_{[1\bar{1}0]} \\ \hat{e}_{[110]} \\ \hat{e}_{[001]} \end{pmatrix}, \tag{A.4}$$

where

$$\tilde{R}(\theta,\phi) = \begin{pmatrix} -\cos\theta\cos\phi & -\cos\theta\sin\phi & \sin\theta \\ -\sin\phi & \cos\phi & 0 \\ -\sin\theta\cos\phi & -\sin\theta\sin\phi & -\cos\theta \end{pmatrix}. \tag{A.5}$$

The basis vectors $\hat{e}_{[1\bar{1}0]}$, $\hat{e}_{[110]}$, and $\hat{e}_{[001]}$ can be expressed as superpositions of the cartesian basis vectors $\hat{e}_{x,[100]}$, $\hat{e}_{y,[010]}$, and $\hat{e}_{z,[001]}$, and can be connected using rotation matrix shown below

$$\begin{pmatrix} \hat{e}_{[1\bar{1}0]} \\ \hat{e}_{[110]} \\ \hat{e}_{[001]} \end{pmatrix} = \begin{pmatrix} \cos 45^\circ & -\sin 45^\circ & 0 \\ \sin 45^\circ & \cos 45^\circ & 0 \\ 0 & 0 & 1 \end{pmatrix} \begin{pmatrix} \hat{e}_x \\ \hat{e}_y \\ \hat{e}_z \end{pmatrix}, \tag{A.6}$$

Thus, the three ortho-normal vectors $\hat{e}_{\mathrm{TM}}$, $\hat{e}_{\mathrm{TE}}$, and $\hat{e}_k$ can be expressed as superpositions of the cartesian basis vectors $\hat{e}_x$, $\hat{e}_y$, and $\hat{e}_z$ as

$$\hat{e}_{\mathrm{TM}} = -\cos\theta\sin(\phi+45\,^\circ)\hat{e}_x + \cos\theta\cos(\phi+45\,^\circ)\hat{e}_y + \sin\theta\ \hat{e}_z \tag{A.7}$$

$$\hat{e}_{\mathrm{TE}} = \cos(\phi+45\,^\circ)\hat{e}_x + \sin(\phi+45\,^\circ)\hat{e}_y \tag{A.8}$$

$$\hat{e}_k = -\sin\theta\sin(\phi+45\,^\circ)\hat{e}_x + \sin\theta\cos(\phi+45\,^\circ)\hat{e}_y - \cos\theta\ \hat{e}_z. \tag{A.9}$$

Thus, the two coordinate systems can be connected using rotation matrix $\tilde{R}(\theta,\phi)$ as

$$\begin{pmatrix} \hat{e}_{\mathrm{TM}} \\ \hat{e}_{\mathrm{TE}} \\ \hat{e}_k \end{pmatrix} = \tilde{R}(\theta,\phi) \begin{pmatrix} \hat{e}_x \\ \hat{e}_y \\ \hat{e}_z \end{pmatrix}, \tag{A.10}$$

where

$$\tilde{R}(\theta,\phi) = \begin{pmatrix} -\cos\theta\sin(\phi+45\,^\circ) & \cos\theta\cos(\phi+45\,^\circ) & \sin\theta \\ \cos(\phi+45\,^\circ) & \sin(\phi+45\,^\circ) & 0 \\ -\sin\theta\sin(\phi+45\,^\circ) & \sin\theta\cos(\phi+45\,^\circ) & -\cos\theta \end{pmatrix}. \tag{A.11}$$

The Cartesian basis vectors $\hat{e}_x$, $\hat{e}_y$, and $\hat{e}_z$ axes can be projected back onto the $\hat{e}_{\mathrm{TM}}$, $\hat{e}_{\mathrm{TE}}$, and $\hat{e}_k$ axes using the inverse matrix $\tilde{R}^{-1}(\theta,\phi)$:

$$\begin{pmatrix} \hat{e}_x \\ \hat{e}_y \\ \hat{e}_z \end{pmatrix} = \tilde{R}^{-1}(\theta,\phi) \begin{pmatrix} \hat{e}_{\mathrm{TM}} \\ \hat{e}_{\mathrm{TE}} \\ \hat{e}_k \end{pmatrix}, \tag{A.12}$$

where

$$\tilde{R}^{-1}(\theta,\phi) = \begin{pmatrix} -\cos\theta\sin(\phi+45\,^\circ) & \cos(\phi+45\,^\circ) & -\sin\theta\sin(\phi+45\,^\circ) \\ \cos\theta\cos(\phi+45\,^\circ) & \sin(\phi+45\,^\circ) & \sin\theta\cos(\phi+45\,^\circ) \\ \sin\theta & 0 & -\cos\theta \end{pmatrix}. \tag{A.13}$$

Thus,

$$\hat{e}_x = -\cos\theta\sin(\phi+45\,^\circ)\hat{e}_{\mathrm{TM}} + \cos(\phi+45\,^\circ)\hat{e}_{\mathrm{TE}} - \sin\theta\sin(\phi+45\,^\circ)\hat{e}_k \tag{A.14}$$

$$\hat{e}_y = \cos\theta\cos(\phi+45\,^\circ)\hat{e}_{\mathrm{TM}} + \sin(\phi+45\,^\circ)\hat{e}_{\mathrm{TE}} + \sin\theta\cos(\phi+45\,^\circ)\hat{e}_k \tag{A.15}$$

$$\hat{e}_z = \sin\theta\ \hat{e}_{\mathrm{TM}} - \cos\theta\ \hat{e}_k. \tag{A.16}$$

A.2 Second Harmonic Generation from GaAs

For GaAs, the only non-zero components of the second-order nonlinear optical susceptibility $\chi^{(2)}$ are

$$\chi^{(2)}_{xyz} = \chi^{(2)}_{xzy} = \chi^{(2)}_{yzx} = \chi^{(2)}_{yxz} = \chi^{(2)}_{zxy} = \chi^{(2)}_{zyx} \equiv \chi^{(2)}_{\text{GaAs}}. \tag{A.17}$$

The i-th component of the induced second harmonic field is written as

$$E_{2\omega,i} = \frac{i\omega l}{n_{2\omega} c\xi} \left[\sum_{j,k} \frac{1}{2} \chi^{(2)}_{ijk} E_{\omega,j} E_{\omega,k} \right] \sin\xi e^{i\xi} \equiv A_{\text{GaAs}} \left[\sum_{j,k} \frac{1}{2} \chi^{(2)}_{ijk} E_{\omega,j} E_{\omega,k} \right], \tag{A.18}$$

where,

$$\vec{E}_\omega = (E_{\omega,x}, E_{\omega,y}, E_{\omega,z}) = E_{\omega,x}\hat{e}_x + E_{\omega,y}\hat{e}_y + E_{\omega,z}\hat{e}_z. \tag{A.19}$$

So, from Equations A.17 and A.18, the x component of the second harmonic is

$$E_{2\omega,x} = A_{\text{GaAs}} \left[\frac{1}{2} (\chi^{(2)}_{xyz} E_{\omega,y} E_{\omega,z} + \chi^{(2)}_{xzy} E_{\omega,z} E_{\omega,y}) \right] = A_{\text{GaAs}} \chi^{(2)}_{\text{GaAs}} E_{\omega,y} E_{\omega,z}. \tag{A.20}$$

And similarly for the y and z components

$$E_{2\omega,y} = A_{\text{GaAs}} \left[\frac{1}{2} (\chi^{(2)}_{yzx} E_{\omega,z} E_{\omega,x} + \chi^{(2)}_{yxz} E_{\omega,x} E_{\omega,z}) \right] = A_{\text{GaAs}} \chi^{(2)}_{\text{GaAs}} E_{\omega,z} E_{\omega,x} \tag{A.21}$$

and

$$E_{2\omega,z} = A_{\text{GaAs}} \left[\frac{1}{2} (\chi^{(2)}_{zxy} E_{\omega,x} E_{\omega,y} + \chi^{(2)}_{zyx} E_{\omega,y} E_{\omega,x}) \right] = A_{\text{GaAs}} \chi^{(2)}_{\text{GaAs}} E_{\omega,x} E_{\omega,y} \tag{A.22}$$

A.2.1 TE excitation

Since the fundamental is only TE polarized

$$\vec{E}_\omega = E_{TE}\hat{e}_{TE} \tag{A.23}$$

Thus from equation rotationTE

$$\vec{E}_\omega = E_{TE}(\cos(\phi + 45\,^\circ)\hat{e}_x + \sin(\phi + 45\,^\circ)\hat{e}_y) \tag{A.24}$$

And from equations A.20 and A.24,

$$E_{2\omega,x} = A_{\text{GaAs}} \chi^{(2)}_{\text{GaAs}} E_{\omega,TE} \sin(\phi + 45\,^\circ) \cdot 0 = 0 \tag{A.25}$$

And similarly for the y and z components

$$E_{2\omega,y} = A_{\text{GaAs}} \chi^{(2)}_{\text{GaAs}} 0 \cdot E_{\omega,TE} \cos(\phi + 45\,^\circ) = 0 \tag{A.26}$$

and

$$\begin{aligned} E_{2\omega,z} &= A_{\text{GaAs}}\chi^{(2)}_{\text{GaAs}}E_{\omega,TE}\sin(\phi+45\,^\circ)\cdot E_{\omega,TE}\cos(\phi+45\,^\circ) \\ &= \frac{1}{2}A_{\text{GaAs}}\chi^{(2)}_{\text{GaAs}}I_{\omega,TE}\sin(2\phi+90\,^\circ) \\ &= \frac{1}{2}A_{\text{GaAs}}\chi^{(2)}_{\text{GaAs}}I_{\omega,TE}\cos 2\phi \end{aligned} \tag{A.27}$$

Thus, the z component is the only nonzero component of the induced SHG

$$\vec{E}_{2\omega} = \frac{1}{2}A_{\text{GaAs}}\chi^{(2)}_{\text{GaAs}}I_{\omega,TE}\cos 2\phi\hat{e}_z \tag{A.28}$$

Using equation A.16, we can project $\hat{e}_z$ back onto the $\hat{e}_{TM}$, $\hat{e}_{TE}$, and $\hat{e}_k$ directions

$$\vec{E}_{2\omega} = \frac{1}{2}A_{\text{GaAs}}\chi^{(2)}_{\text{GaAs}}I_{\omega,TE}\cos 2\phi(\sin\theta\ \hat{e}_{\text{TM}} - \cos\theta\ \hat{e}_k) \tag{A.29}$$

For TM polarized SHG

$$E_{2\omega,TM} = \frac{1}{2}A_{\text{GaAs}}\chi^{(2)}_{\text{GaAs}}I_{\omega,TE}\cos 2\phi\sin\theta \tag{A.30}$$

The incident fundamental is refracted, after entering the the sample at $\theta_{ext} = 45\,^\circ$. The refractive index of GaAs is $n_{\text{GaAs}} = 3.857$, thus

$$\begin{aligned} n_{\text{Air}}\sin\theta_{ext} &= n_{\text{GaAs}}\sin\theta_{int} \\ \sin 45\,^\circ &= 3.857\sin\theta_{int} \\ \Rightarrow \theta_{int} \equiv \theta &= 10.56\,^\circ \end{aligned} \tag{A.31}$$

Thus, the fundamental propagates through the GaAs substrate at $10.56\,^\circ$, so

$$E_{2\omega,TM} = \frac{1}{2}\sin(10.56\,^\circ)A_{\text{GaAs}}\chi^{(2)}_{\text{GaAs}}I_{\omega,TE}\cos 2\phi \tag{A.32}$$

A.2.2 TM excitation

When the fundamental is TM polarized

$$\vec{E}_\omega = E_{TM}\hat{e}_{TM} \tag{A.33}$$

Thus from equation A.8

$$\vec{E}_\omega = E_{TM}(-\cos\theta\sin(\phi+45\,^\circ)\hat{e}_x + \cos\theta\cos(\phi+45\,^\circ)\hat{e}_y + \sin\theta\ \hat{e}_z) \tag{A.34}$$

And from equation A.20 and A.34

$$\begin{aligned} E_{2\omega,x} &= A_{\mathrm{GaAs}}\chi^{(2)}_{\mathrm{GaAs}}E_{\omega,\mathrm{TM}}\cos\theta\cos(\phi+45\,^\circ)\cdot E_{\omega,TM}\sin\theta \\ &= \frac{1}{2}A_{\mathrm{GaAs}}\chi^{(2)}_{\mathrm{GaAs}}I_{\omega,TM}\sin 2\theta\cos(\phi+45\,^\circ) \end{aligned} \tag{A.35}$$

And similarly for the y and z components

$$\begin{aligned} E_{2\omega,y} &= -A_{\mathrm{GaAs}}\chi^{(2)}_{\mathrm{GaAs}}E_{\omega,TM}\sin\theta\cdot E_{\omega,TM}\cos\theta\sin(\phi+45\,^\circ) \\ &= -\frac{1}{2}A_{\mathrm{GaAs}}\chi^{(2)}_{\mathrm{GaAs}}I_{\omega,TM}\sin 2\theta\sin(\phi+45\,^\circ) \end{aligned} \tag{A.36}$$

and

$$\begin{aligned} E_{2\omega,z} &= -A_{\mathrm{GaAs}}\chi^{(2)}_{\mathrm{GaAs}}E_{\omega,TM}\cos\theta\sin(\phi+45\,^\circ)\cdot E_{\omega,TM}\cos\theta\cos(\phi+45\,^\circ) \\ &= -\frac{1}{2}A_{\mathrm{GaAs}}\chi^{(2)}_{\mathrm{GaAs}}I_{\omega,TM}\cos^2\theta\sin(2\phi+90\,^\circ) \\ &= -\frac{1}{2}A_{\mathrm{GaAs}}\chi^{(2)}_{\mathrm{GaAs}}I_{\omega,TM}\cos^2\theta\cos 2\phi \end{aligned} \tag{A.37}$$

Thus

$$\vec{E}_{2\omega} = \frac{1}{2}A_{\mathrm{GaAs}}\chi^{(2)}_{\mathrm{GaAs}}I_{\omega,TM}(\sin 2\theta\cos(\phi+45\,^\circ)\hat{e}_x - \sin 2\theta\sin(\phi+45\,^\circ)\hat{e}_y - \cos^2\theta\cos 2\phi\hat{e}_z) \tag{A.38}$$

Thus using equations A.15 - A.16, we can project these Cartesian components back onto the $\hat{e}_{TM}$,$\hat{e}_{TE}$, and $\hat{e}_k$ directions, and the TM and TE components of the induced SHG can be resolved. For TM polarized SHG

$$\begin{aligned} E_{2\omega,TM} &= \frac{1}{2}A_{\mathrm{GaAs}}\chi^{(2)}_{\mathrm{GaAs}}I_{\omega,TM}(-\sin 2\theta\cos(\phi+45\,^\circ)\cos\theta\sin(\phi+45\,^\circ) \\ &\quad -\sin 2\theta\sin(\phi+45\,^\circ)\cos\theta\cos(\phi+45\,^\circ) - \cos^2\theta\cos 2\phi\sin\theta) \\ &= -\frac{3}{4}A_{\mathrm{GaAs}}\chi^{(2)}_{\mathrm{GaAs}}I_{\omega,TM}\sin 2\theta\cos 2\phi\cos\theta \end{aligned} \tag{A.39}$$

but, $\theta = 10.56\,^\circ$, thus

$$E_{2\omega,TM} = -\frac{3}{4}\cos 10.56\,^\circ\sin 21.12\,^\circ A_{\mathrm{GaAs}}\chi^{(2)}_{\mathrm{GaAs}}I_{\omega,TM}\cos 2\phi \tag{A.40}$$

Similarly for TE polarized SHG

$$\begin{aligned} E_{2\omega,TE} &= \frac{1}{2}A_{\mathrm{GaAs}}\chi^{(2)}_{\mathrm{GaAs}}I_{\omega,TM}(\sin 2\theta\cos(\phi+45\,^\circ)\cos(\phi+45\,^\circ) - \sin 2\theta\sin(\phi+45\,^\circ)\sin(\phi+45\,^\circ) \\ &= -\frac{1}{2}A_{\mathrm{GaAs}}\chi^{(2)}_{\mathrm{GaAs}}I_{\omega,TM}\sin 2\theta\cos(2\phi+90\,^\circ) \\ &= -\frac{1}{2}A_{\mathrm{GaAs}}\chi^{(2)}_{\mathrm{GaAs}}I_{\omega,TM}\sin 2\theta\sin 2\phi \end{aligned} \tag{A.41}$$

but, $\theta = 10.56\,°$, thus

$$E_{2\omega,TE} = \frac{1}{2}\sin 21.12\,° A_{\mathrm{GaAs}} \chi^{(2)}_{\mathrm{GaAs}} I_{\omega,TM} \sin 2\phi \tag{A.42}$$

A.3 Second Harmonic Generation from GaAs Including Linear Absorption from CNTs

The highly aligned CNTs act as a imperfect polarizer in the mid-IR. Thus the components of the incident fundamental perpendicualar and parallel to the axis of the CNTs undergo anisotropic transmission. The transmission Jones matrix, $\tilde{T}_{CNT}$, for such a polarizing element is

$$\tilde{T}_{CNT} = \begin{pmatrix} \sqrt{\%T_\perp} & 0 & 0 \\ 0 & \sqrt{\%T_\parallel} & 0 \\ 0 & 0 & 1 \end{pmatrix}. \tag{A.43}$$

Thus, from equation A.10 the initial incident fundamental E field is

$$\vec{E}_{\omega,0} = \begin{pmatrix} E_{\mathrm{TM}} \\ E_{\mathrm{TE}} \\ E_k \end{pmatrix} = \begin{pmatrix} -\cos\theta\cos\phi & -\cos\theta\sin\phi & \sin\theta \\ -\sin\phi & \cos\phi & 0 \\ -\sin\theta\cos\phi & -\sin\theta\sin\phi & -\cos\theta \end{pmatrix} \begin{pmatrix} E_{[1\bar{1}0]} \\ E_{[110]} \\ E_{[001]} \end{pmatrix}. \tag{A.44}$$

And the final (transmitted through CNTs) incident fundamental E field is

$$\begin{aligned} \vec{E}_{\omega,f} = \begin{pmatrix} E_{\mathrm{TM}} \\ E_{\mathrm{TE}} \\ E_k \end{pmatrix} &= \begin{pmatrix} \sqrt{\%T_\perp} & 0 & 0 \\ 0 & \sqrt{\%T_\parallel} & 0 \\ 0 & 0 & 1 \end{pmatrix} \begin{pmatrix} -\cos\theta\cos\phi & -\cos\theta\sin\phi & \sin\theta \\ -\sin\phi & \cos\phi & 0 \\ -\sin\theta\cos\phi & -\sin\theta\sin\phi & -\cos\theta \end{pmatrix} \begin{pmatrix} E_{[1\bar{1}0]} \\ E_{[110]} \\ E_{[001]} \end{pmatrix} \\ &= \begin{pmatrix} -\sqrt{\%T_\perp}\cos\theta\cos\phi & -\sqrt{\%T_\parallel}\cos\theta\sin\phi & \sin\theta \\ -\sqrt{\%T_\perp}\sin\phi & \sqrt{\%T_\parallel}\cos\phi & 0 \\ -\sqrt{\%T_\perp}\sin\theta\cos\phi & -\sqrt{\%T_\parallel}\sin\theta\sin\phi & -\cos\theta \end{pmatrix} \begin{pmatrix} E_{[1\bar{1}0]} \\ E_{[110]} \\ E_{[001]} \end{pmatrix}. \end{aligned} \tag{A.45}$$

Using equation ?? we can project $\vec{E}_{\omega,f}$ onto the $\hat{e}_{x,[100]}$, $\hat{e}_{y,[010]}$, and $\hat{e}_{z,[001]}$ directions

$$\begin{pmatrix} E_{\mathrm{TM}} \\ E_{\mathrm{TE}} \\ E_k \end{pmatrix} = \begin{pmatrix} \frac{-\cos\theta(\sqrt{\%T_\perp}\cos\phi+\sqrt{\%T_\parallel}\sin\phi)}{\sqrt{2}} & \frac{-\cos\theta(\sqrt{\%T_\perp}\cos\phi-\sqrt{\%T_\parallel}\sin\phi)}{\sqrt{2}} & \sin\theta \\ \frac{(\sqrt{\%T_\parallel}\cos\phi-\sqrt{\%T_\perp}\sin\phi)}{\sqrt{2}} & \frac{(\sqrt{\%T_\parallel}\cos\phi+\sqrt{\%T_\perp}\sin\phi)}{\sqrt{2}} & 0 \\ \frac{-\sin\theta(\sqrt{\%T_\perp}\cos\phi+\sqrt{\%T_\parallel}\sin\phi)}{\sqrt{2}} & \frac{\sin\theta(\sqrt{\%T_\perp}\cos\phi-\sqrt{\%T_\parallel}\sin\phi)}{\sqrt{2}} & -\cos\theta \end{pmatrix} \begin{pmatrix} E_x \\ E_y \\ E_z \end{pmatrix} \tag{A.46}$$

A.3.1 TE excitation

Since the fundamental is only TE polarized

$$\vec{E}_\omega = E_{TE}\hat{e}_{TE} \tag{A.47}$$

Thus from equation A.46

$$\vec{E}_\omega = E_{TE}\left(\frac{\sqrt{\%T_\parallel}\cos\phi - \sqrt{\%T_\perp}\sin\phi}{\sqrt{2}}\hat{e}_x + \frac{\sqrt{\%T_\parallel}\cos\phi + \sqrt{\%T_\perp}\sin\phi}{\sqrt{2}}\hat{e}_y\right) \tag{A.48}$$

And from equations A.20 and A.48,

$$E_{2\omega,x} = A_{\mathrm{GaAs}}\chi^{(2)}_{\mathrm{GaAs}}E_{\omega,TE}\frac{\sqrt{\%T_\parallel}\cos\phi + \sqrt{\%T_\perp}\sin\phi}{\sqrt{2}}\cdot 0 = 0 \tag{A.49}$$

And similarly for the y and z components

$$E_{2\omega,y} = A_{\mathrm{GaAs}}\chi^{(2)}_{\mathrm{GaAs}}0\cdot E_{\omega,TE}\frac{\sqrt{\%T_\parallel}\cos\phi - \sqrt{\%T_\perp}\sin\phi}{\sqrt{2}} = 0 \tag{A.50}$$

and

$$\begin{aligned} E_{2\omega,z} &= A_{\mathrm{GaAs}}\chi^{(2)}_{\mathrm{GaAs}}E_{\omega,TE}\frac{\sqrt{\%T_\parallel}\cos\phi - \sqrt{\%T_\perp}\sin\phi}{\sqrt{2}}\cdot E_{\omega,TE}\frac{\sqrt{\%T_\parallel}\cos\phi + \sqrt{\%T_\perp}\sin\phi}{\sqrt{2}} \\ &= \frac{1}{2}A_{\mathrm{GaAs}}\chi^{(2)}_{\mathrm{GaAs}}I_{\omega,TE}\left[(\%T_\parallel)\cos^2\phi - (\%T_\perp)\sin^2\phi\right] \end{aligned} \tag{A.51}$$

Thus, the z component is the only nonzero component of the induced SHG

$$\vec{E}_{2\omega} = \frac{1}{2}A_{\mathrm{GaAs}}\chi^{(2)}_{\mathrm{GaAs}}I_{\omega,TE}\left[(\%T_\parallel)\cos^2\phi - (\%T_\perp)\sin^2\phi\right]\hat{e}_z \tag{A.52}$$

Using equation A.16, we can project $\hat{e}_z$ back onto the $\hat{e}_{TM}$, $\hat{e}_{TE}$, and $\hat{e}_k$ directions

$$\vec{E}_{2\omega} = \frac{1}{2}A_{\mathrm{GaAs}}\chi^{(2)}_{\mathrm{GaAs}}I_{\omega,TE}\left[(\%T_\parallel)\cos^2\phi - (\%T_\perp)\sin^2\phi\right](\sin\theta\ \hat{e}_{\mathrm{TM}} - \cos\theta\ \hat{e}_k) \tag{A.53}$$

Thus for TM polarized SHG

$$E_{2\omega,TM} = \frac{1}{2}A_{\mathrm{GaAs}}\chi^{(2)}_{\mathrm{GaAs}}I_{\omega,TE}\left[(\%T_\parallel)\cos^2\phi - (\%T_\perp)\sin^2\phi\right]\sin\theta \tag{A.54}$$

Because, the fundamental propagates through the GaAs substrate at 10.56 °, so

$$E_{2\omega,TM} = \frac{1}{2}\sin(10.56\,^\circ)A_{\mathrm{GaAs}}\chi^{(2)}_{\mathrm{GaAs}}I_{\omega,TE}\left[(\%T_\parallel)\cos^2\phi - (\%T_\perp)\sin^2\phi\right] \tag{A.55}$$

A.3.2 TM excitation

When the fundamental is TM polarized

$$\vec{E}_\omega = E_{TM}\hat{e}_{TM} \tag{A.56}$$

Thus from equation A.46

$$\vec{E}_\omega = E_{TM}(-\frac{\cos\theta(\sqrt{\%T_\perp}\cos\phi + \sqrt{\%T_\parallel}\sin\phi)}{\sqrt{2}}\hat{e}_x + \frac{\cos\theta(\sqrt{\%T_\perp}\cos\phi - \sqrt{\%T_\parallel}\sin\phi)}{\sqrt{2}}\hat{e}_y + \sin\theta\ \hat{e}_z) \tag{A.57}$$

And from equation A.20 and A.57

$$\begin{aligned} E_{2\omega,x} &= A_{\mathrm{GaAs}}\chi^{(2)}_{\mathrm{GaAs}}E_{\omega,\mathrm{TM}}\frac{\cos\theta(\sqrt{\%T_\perp}\cos\phi - \sqrt{\%T_\parallel}\sin\phi)}{\sqrt{2}}\cdot E_{\omega,TM}\sin\theta \\ &= \frac{1}{2}A_{\mathrm{GaAs}}\chi^{(2)}_{\mathrm{GaAs}}I_{\omega,TM}\sin 2\theta\frac{\sqrt{\%T_\perp}\cos\phi - \sqrt{\%T_\parallel}\sin\phi}{\sqrt{2}} \end{aligned} \tag{A.58}$$

And similarly for the y and z components

$$\begin{aligned} E_{2\omega,y} &= -A_{\mathrm{GaAs}}\chi^{(2)}_{\mathrm{GaAs}}E_{\omega,TM}\sin\theta\cdot E_{\omega,TM}\frac{\cos\theta(\sqrt{\%T_\perp}\cos\phi + \sqrt{\%T_\parallel}\sin\phi)}{\sqrt{2}} \\ &= -\frac{1}{2}A_{\mathrm{GaAs}}\chi^{(2)}_{\mathrm{GaAs}}I_{\omega,TM}\sin 2\theta\frac{\sqrt{\%T_\perp}\cos\phi + \sqrt{\%T_\parallel}\sin\phi}{\sqrt{2}} \end{aligned} \tag{A.59}$$

and

$$\begin{aligned} E_{2\omega,z} &= -A_{\mathrm{GaAs}}\chi^{(2)}_{\mathrm{GaAs}}E_{\omega,TM}\frac{\cos\theta(\sqrt{\%T_\perp}\cos\phi + \sqrt{\%T_\parallel}\sin\phi)}{\sqrt{2}}\cdot E_{\omega,TM}\frac{\cos\theta(\sqrt{\%T_\perp}\cos\phi - \sqrt{\%T_\parallel}\sin\phi)}{\sqrt{2}} \\ &= -\frac{1}{2}A_{\mathrm{GaAs}}\chi^{(2)}_{\mathrm{GaAs}}I_{\omega,TM}\cos^2\theta\left[(\%T_\perp)\cos^2\phi - (\%T_\parallel)\sin^2\phi\right] \end{aligned} \tag{A.60}$$

Thus

$$\begin{aligned} \vec{E}_{2\omega} &= \frac{1}{2}A_{\mathrm{GaAs}}\chi^{(2)}_{\mathrm{GaAs}}I_{\omega,TM}(\sin 2\theta\frac{\sqrt{\%T_\perp}\cos\phi - \sqrt{\%T_\parallel}\sin\phi}{\sqrt{2}}\hat{e}_x \\ &\quad - \sin 2\theta\frac{\sqrt{\%T_\perp}\cos\phi + \sqrt{\%T_\parallel}\sin\phi}{\sqrt{2}}\hat{e}_y \\ &\quad - \cos^2\theta\left[(\%T_\perp)\cos^2\phi - (\%T_\parallel)\sin^2\phi\right]\hat{e}_z) \end{aligned} \tag{A.61}$$

Thus using equations A.15 - A.16, we can project these Cartesian components back onto the $\hat{e}_{TM}$ and $\hat{e}_{TE}$ directions

$$\vec{E}_{2\omega} = \frac{1}{2}A_{\mathrm{GaAs}}\chi^{(2)}_{\mathrm{GaAs}}I_{\omega,TM}\begin{bmatrix} \sin 2\theta\frac{\sqrt{\%T_\perp}\cos\phi - \sqrt{\%T_\parallel}\sin\phi}{\sqrt{2}}(-\cos\theta\sin(\phi+45\,^\circ)\hat{e}_{\mathrm{TM}} + \cos(\phi+45\,^\circ)\hat{e}_{\mathrm{TE}}) \\ -\sin 2\theta\frac{\sqrt{\%T_\perp}\cos\phi + \sqrt{\%T_\parallel}\sin\phi}{\sqrt{2}}(\cos\theta\cos(\phi+45\,^\circ)\hat{e}_{\mathrm{TM}} + \sin(\phi+45\,^\circ)\hat{e}_{\mathrm{TE}}) \\ -\cos^2\theta\left[(\%T_\perp)\cos^2\phi - (\%T_\parallel)\sin^2\phi\right](\sin\theta\ \hat{e}_{\mathrm{TM}}) \end{bmatrix} \tag{A.62}$$

For TM polarized SHG

$$\begin{aligned} E_{2\omega,TM} &= \frac{1}{2}A_{\mathrm{GaAs}}\chi^{(2)}_{\mathrm{GaAs}}I_{\omega,TM}\begin{bmatrix} \sin 2\theta\frac{\sqrt{\%T_\perp}\cos\phi-\sqrt{\%T_\parallel}\sin\phi}{\sqrt{2}}(-\cos\theta\sin(\phi+45\,^\circ)) \\ -\sin 2\theta\frac{\sqrt{\%T_\perp}\cos\phi+\sqrt{\%T_\parallel}\sin\phi}{\sqrt{2}}(\cos\theta\cos(\phi+45\,^\circ)) \\ -\cos^2\theta\left[(\%T_\perp)\cos^2\phi-(\%T_\parallel)\sin^2\phi\right](\sin\theta) \end{bmatrix} \\ &= -\frac{1}{4}A_{\mathrm{GaAs}}\chi^{(2)}_{\mathrm{GaAs}}I_{\omega,TM}\sin 2\theta\cos\theta\begin{bmatrix} 2\sqrt{\%T_\perp}+\%T_\perp-2\sqrt{\%T_\parallel}-\%T_\parallel \\ +(2\sqrt{\%T_\perp}+\%T_\perp+2\sqrt{\%T_\parallel}+\%T_\parallel)\cos 2\phi \end{bmatrix} \end{aligned} \tag{A.63}$$

Similarly for TE polarized SHG

$$\begin{aligned} E_{2\omega,TE} &= \frac{1}{2}A_{\mathrm{GaAs}}\chi^{(2)}_{\mathrm{GaAs}}I_{\omega,TE}\begin{bmatrix} \sin 2\theta\frac{\sqrt{\%T_\perp}\cos\phi-\sqrt{\%T_\parallel}\sin\phi}{\sqrt{2}}(\cos(\phi+45\,^\circ)) \\ -\sin 2\theta\frac{\sqrt{\%T_\perp}\cos\phi+\sqrt{\%T_\parallel}\sin\phi}{\sqrt{2}}(\sin(\phi+45\,^\circ)) \end{bmatrix} \\ &= -\frac{1}{4}A_{\mathrm{GaAs}}\chi^{(2)}_{\mathrm{GaAs}}I_{\omega,TE}\sin 2\theta(\sqrt{\%T_\parallel}-\sqrt{\%T_\perp})\sin 2\phi \end{aligned} \tag{A.64}$$

but, $\theta = 10.56\,^\circ$, thus

$$E_{2\omega,TE} = \frac{1}{4}\sin 21.12\,^\circ A_{\mathrm{GaAs}}\chi^{(2)}_{\mathrm{GaAs}}I_{\omega,TM}(\sqrt{\%T_\parallel}-\sqrt{\%T_\perp})\sin 2\phi \tag{A.65}$$

A.4 Second Harmonic Generation from Carbon Nanotubes

The three ortho-normal vectors $\hat{e}_{\mathrm{TM}}$, $\hat{e}_{\mathrm{TE}}$, and $\hat{e}_k$ can be expressed as superpositions of the cartesian basis vectors $\hat{e}_x$, $\hat{e}_y$, and $\hat{e}_z$ as

$$\hat{e}_{\mathrm{TM}} = \sin\theta\hat{e}_x - \cos\theta\cos\phi\hat{e}_y - \cos\theta\sin\phi\hat{e}_z \tag{A.66}$$

$$\hat{e}_{\mathrm{TE}} = -\sin\phi\hat{e}_y + \cos\phi\hat{e}_z \tag{A.67}$$

$$\hat{e}_k = -\cos\theta\hat{e}_x - \sin\theta\cos\phi\hat{e}_y - \sin\theta\sin\phi\hat{e}_z \tag{A.68}$$

Thus, the two coordinate systems can be connected using rotation matrix $\tilde{R}(\theta,\phi)$ as

$$\begin{pmatrix} \hat{e}_{\mathrm{TM}} \\ \hat{e}_{\mathrm{TE}} \\ \hat{e}_k \end{pmatrix} = \tilde{R}(\theta,\phi)\begin{pmatrix} \hat{e}_x \\ \hat{e}_y \\ \hat{e}_z \end{pmatrix}, \tag{A.69}$$

where

$$\tilde{R}(\theta,\phi) = \begin{pmatrix} \sin\theta & -\cos\theta\cos\phi & -\cos\theta\sin\phi \\ 0 & -\sin\phi & \cos\phi \\ -\cos\theta & -\sin\theta\cos\phi & -\sin\theta\sin\phi \end{pmatrix}. \tag{A.70}$$

The Cartesian basis vectors $\hat{e}_x$, $\hat{e}_y$, and $\hat{e}_z$ axes can be projected back onto the $\hat{e}_{\mathrm{TM}}$, $\hat{e}_{\mathrm{TE}}$, and $\hat{e}_k$ axes using the inverse matrix $\tilde{R}^{-1}(\theta,\phi)$:

$$\begin{pmatrix} \hat{e}_x \\ \hat{e}_y \\ \hat{e}_z \end{pmatrix} = \tilde{R}^{-1}(\theta,\phi) \begin{pmatrix} \hat{e}_{\mathrm{TM}} \\ \hat{e}_{\mathrm{TE}} \\ \hat{e}_k \end{pmatrix}, \tag{A.71}$$

where

$$\tilde{R}^{-1}(\theta,\phi) = \begin{pmatrix} \sin\theta & 0 & -\cos\theta \\ -\cos\theta\cos\phi & -\sin\phi & -\sin\theta\cos\phi \\ -\cos\theta\sin\phi & \cos\phi & -\sin\theta\sin\phi \end{pmatrix}. \tag{A.72}$$

Thus,

$$\hat{e}_x = \sin\theta\hat{e}_{\mathrm{TM}} - \cos\theta\hat{e}_k \tag{A.73}$$

$$\hat{e}_y = -\cos\theta\cos\phi\hat{e}_{\mathrm{TM}} - \sin\phi\hat{e}_{\mathrm{TE}} - \sin\theta\cos\phi\hat{e}_k \tag{A.74}$$

$$\hat{e}_z = -\cos\theta\sin\phi\hat{e}_{\mathrm{TM}} + \cos\phi\hat{e}_{\mathrm{TE}} - \sin\theta\sin\phi\hat{e}_k \tag{A.75}$$

For carbon nanotubes

$$\chi^{(2)}_{xyz} = -\chi^{(2)}_{yzx} = \chi^{(2)}_{\mathrm{CNT}} \tag{A.76}$$

So, from equation A.18, the x component of the induced SHG is,

$$E_{2\omega,x} = A_{\mathrm{CNT}}\left[\frac{1}{2}(\chi^{(2)}_{xyz}E_{\omega,y}E_{\omega,z} + \chi^{(2)}_{xzy}E_{\omega,z}E_{\omega,y})\right] = \frac{1}{2}A_{\mathrm{CNT}}\chi^{(2)}_{\mathrm{CNT}}E_{\omega,y}E_{\omega,z}. \tag{A.77}$$

and the y component is,

$$E_{2\omega,y} = A_{\mathrm{CNT}}\left[\frac{1}{2}(\chi^{(2)}_{yzx}E_{\omega,z}E_{\omega,x} + \chi^{(2)}_{yxz}E_{\omega,x}E_{\omega,z})\right] = \frac{1}{2}A_{\mathrm{CNT}}\chi^{(2)}_{\mathrm{CNT}}E_{\omega,z}E_{\omega,x} \tag{A.78}$$

A.4.1 TE excitation

When the fundamental is only TE polarized

$$\vec{E}_\omega = E_{TE}\hat{e}_{TE} \tag{A.79}$$

Thus from equation A.68

$$\vec{E}_\omega = E_{TE}(-\sin\phi\hat{e}_y + \cos\phi\hat{e}_z) \tag{A.80}$$

And from equations A.77 and A.80,

$$\begin{aligned} E_{2\omega,x} &= \frac{1}{2}A_{\mathrm{CNT}}\chi^{(2)}_{\mathrm{CNT}}E_{\omega,TE}(-\sin\phi)\cdot(\cos\phi) \\ &= -\frac{1}{4}A_{\mathrm{CNT}}\chi^{(2)}_{\mathrm{CNT}}E^2_{\omega,TE}\sin 2\phi \end{aligned} \tag{A.81}$$

And similarly for y component

$$E_{2\omega,y} = \frac{1}{2} A_{\mathrm{CNT}} \chi^{(2)}_{\mathrm{CNT}} E_{\omega,TE} \cos\phi \cdot 0 = 0 \tag{A.82}$$

Thus, the x component is the only nonzero component of the induced SHG

$$\vec{E}_{2\omega} = -\frac{1}{4} A_{\mathrm{CNT}} \chi^{(2)}_{\mathrm{CNT}} I_{\omega,TE} \sin 2\phi \hat{e}_x \tag{A.83}$$

Using equation A.74, we can project $\hat{e}_x$ back onto the $\hat{e}_{TM}$, $\hat{e}_{TE}$, and $\hat{e}_k$ directions

$$\vec{E}_{2\omega} = -\frac{1}{4} A_{\mathrm{CNT}} \chi^{(2)}_{\mathrm{CNT}} I_{\omega,TE} \sin 2\phi (\sin\theta \hat{e}_{\mathrm{TM}} - \cos\theta \hat{e}_k) \tag{A.84}$$

For TM polarized SHG

$$E_{2\omega,TM} = -\frac{1}{4} A_{\mathrm{CNT}} \chi^{(2)}_{\mathrm{CNT}} I_{\omega,TE} \sin 2\phi \sin\theta \tag{A.85}$$

but, $\theta = 45\,^\circ$, thus

$$E_{2\omega,TM} = -\frac{1}{4\sqrt{2}} A_{\mathrm{CNT}} \chi^{(2)}_{\mathrm{CNT}} I_{\omega,TE} \sin 2\phi \tag{A.86}$$

A.4.2 TM excitation

When the fundamental is TM polarized

$$\vec{E}_{\omega} = E_{TM} \hat{e}_{TM} \tag{A.87}$$

Thus from equation A.68

$$\vec{E}_{\omega} = E_{TM} (\sin\theta \hat{e}_x - \cos\theta \cos\phi \hat{e}_y - \cos\theta \sin\phi \hat{e}_z) \tag{A.88}$$

And from equation A.20 and A.88

$$\begin{aligned} E_{2\omega,x} &= \frac{1}{2} A_{\mathrm{CNT}} \chi^{(2)}_{\mathrm{CNT}} E_{\omega,TM} \cos\theta \cos\phi \cdot E_{\omega,TM} \cos\theta \sin\phi \\ &= \frac{1}{4} A_{\mathrm{CNT}} \chi^{(2)}_{\mathrm{CNT}} I_{\omega,TM} \cos^2\theta \sin 2\phi \end{aligned} \tag{A.89}$$

And similarly for the y component

$$\begin{aligned} E_{2\omega,y} &= -\frac{1}{2} A_{\mathrm{CNT}} \chi^{(2)}_{\mathrm{CNT}} E_{\omega,TM} \cos\theta \sin\phi \cdot E_{\omega,TM} \sin\theta \\ &= -\frac{1}{4} A_{\mathrm{CNT}} \chi^{(2)}_{\mathrm{CNT}} I_{\omega,TM} \sin 2\theta \sin\phi \end{aligned} \tag{A.90}$$

thus,

$$\vec{E}_{2\omega} = \frac{1}{4} A_{\mathrm{CNT}} \chi^{(2)}_{\mathrm{CNT}} I_{\omega,TM} (\cos^2\theta \sin 2\phi \hat{e}_x - \sin 2\theta \sin\phi \hat{e}_y) \tag{A.91}$$

Thus using equations A.15 - A.16, we can project these Cartesian components back onto the $\hat{e}_{TM}$,$\hat{e}_{TE}$, and $\hat{e}_k$ directions thus,

$$\vec{E}_{2\omega} = \frac{1}{4}A_{\mathrm{CNT}}\chi^{(2)}_{\mathrm{CNT}}I_{\omega,TM}(-\cos^2\theta\sin 2\phi(\sin\theta\hat{e}_{\mathrm{TM}} - \cos\theta\hat{e}_k) \tag{A.92}$$

$$-\sin 2\theta\sin\phi(-\cos\theta\cos\phi\hat{e}_{\mathrm{TM}} - \sin\phi\hat{e}_{\mathrm{TE}} - \sin\theta\cos\phi\hat{e}_k)) \tag{A.93}$$

For TM polarized SHG

$$E_{2\omega,TM} = \frac{1}{4}A_{\mathrm{CNT}}\chi^{(2)}_{\mathrm{CNT}}I_{\omega,TM}(-\cos^2\theta\sin 2\phi\sin\theta + \sin 2\theta\sin\phi\cos\theta\cos\phi$$

$$= -\frac{1}{8}A_{\mathrm{CNT}}\chi^{(2)}_{\mathrm{CNT}}I_{\omega,TM}(-\sin 2\theta\cos\theta\sin 2\phi + \sin 2\theta\cos\theta\sin 2\phi) = 0 \tag{A.94}$$

$$\tag{A.95}$$

Similarly for TE polarized SHG

$$E_{2\omega,TE} = -\frac{1}{4}A_{\mathrm{CNT}}\chi^{(2)}_{\mathrm{CNT}}I_{\omega,TM}\sin 2\theta\sin\phi\sin\phi \tag{A.96}$$

$$= -\frac{1}{4}A_{\mathrm{CNT}}\chi^{(2)}_{\mathrm{CNT}}I_{\omega,TM}\sin 2\theta\sin^2\phi \tag{A.97}$$

but, $\theta = 45\,^\circ$, thus

$$E_{2\omega,TE} = -\frac{1}{4}A_{\mathrm{CNT}}\chi^{(2)}_{\mathrm{CNT}}I_{\omega,TM}\sin^2\phi \tag{A.98}$$

Bibliography

[1] A. K. Geim and K. S. Novoselov, "The rise of graphene," Nature Mater. **6**, 183 (2007).

[2] A. B. Kuzmenko, E. van Heumen, F. Carbone, and D. van der Marel, "Universal Optical Conductance of Graphite," Phys. Rev. Lett. **100**, 117401 (Mar 2008).

[3] F. Schedin, A. K. Geim, S. V. Morozov, E. W. Hill, P. Blake, M. I. Katsnelson, and K. S. Novoselov, "Detection of individual gas molecules adsorbed on graphene," Nature Mater. **6**, 652 (2007).

[4] K. S. Novoselov, A. K. Geim, S. V. Morozov, D. Jiang, Y. Zhang, S. Dubonos, I. V. Grigorieva, and A. A. Firsov, "Electric Field Effect in Atomically Thin Carbon Films," Science **306**, 666 (2004).

[5] M. D. Stoller, S. Park, Y. Zhu, J. An, and R. S. Ruoff, "Graphene-Based Ultracapacitors," Nano Lett. **8**, 3498 (2008), pMID: 18788793.

[6] F. Xia, T. Mueller, Y. Lin, A. Valdes-Garcia, and P. Avouris, "Ultrafast graphene photodetector," Nat. Nanotechnol. **4**, 839 (2009).

[7] H. W. C. Postma, T. Teepen, Z. Yao, M. Grifoni, and C. Dekker, "Carbon Nanotube Single-Electron Transistors at Room Temperature," Science **293**, 76 (2001).

[8] E. S. Snow, F. K. Perkins, E. J. Houser, S. C. Badescu, and T. L. Reinecke, "Chemical Detection with a Single-Walled Carbon Nanotube Capacitor," Science

307, 1942 (2005).

[9] T. W. Odom, J. L. Huang, P. Kim, and C. M. Lieber, "Structure and Electronic Properties of Carbon Nanotubes," J.Phys. Chem. B **104**, 2794 (2000).

[10] P. Avouris, Z. Chen, and V. Perebeinos, "Carbon-based electronics," Nat. Nanotechnol. **2**, 605 (2007).

[11] M. Dresselhaus, G. Dresselhaus, and A. J. R. Saito, "Raman spectroscopy of carbon nanotubes," (2005).

[12] K. V. Christ and H. R. Sadeghpour, "Energy dispersion in graphene and carbon nanotubes and molecular encapsulation in nanotubes," Phys. Rev. B **75**, 195418 (2007).

[13] H. Kataura, Y. Kumazawa, Y. Maniwa, I. Umezu, S. Suzuki, Y. Ohtsuka, and Y. Achiba, "Optical properties of single-wall carbon nanotubes," Synth. Mater. **103**, 2555 (1999), international Conference on Science and Technology of Synthetic Metals.

[14] A. Hagen and T. Hertel, "Quantitative Analysis of Optical Spectra from Individual Single-Wall Carbon Nanotubes," Nano Lett. **3**, 383 (2003).

[15] J. Lefebvre, S. Maruyama, and P. Finnie, "Photoluminescence: Science and Applications," in *Carbon Nanotubes* (Springer Berlin / Heidelberg, 2008), vol. 111 of *Topics in Applied Physics*, pp. 287–319, 10.1007/978-3-540-72865-8.

[16] S. M. Bachilo, M. Sergei, M. S. Strano, C. Kittrell, R. H. Hauge, R. E. Smalley, and R. B. Weisman, "Structure-Assigned Optical Spectra of Single-Walled Carbon Nanotubes," Science **298**, 2361 (2002).

[17] A. Jorio and M. S. Dresselhaus, editors, *Carbon Nanotubes Advanced Topics in the Synthesis, Structure, Properties and Applications* (Springer, 2008).

[18] R. W. Boyd, editor, *Nonlinear Optics: 2nd Edition* (Academic Press, 2003).

[19] P. N. Butcher and D. Cotter, editors, *The Elements of Nonliner Optics* (Cambridge University Press, 1990).

[20] G. Y. Guo, K. C. Chu, D.-s. Wang, and C.-g. Duan, "Linear and nonlinear optical properties of carbon nanotubes from first-principles calculations," Phys. Rev. B **69**, 205416 (May 2004).

[21] V. A. Margulis, E. A. Gaiduk, and E. N. Zhidkin, "Quadratic electro-optic effects in semiconductor carbon nanotubes," Phys. Lett. A **258**, 394 (1999).

[22] V. A. Margulis and E. A. Gaiduk, "Theoretical modelling of nonlinear refraction and two-photon absorption in single-wall carbon nanotube bundles," J. Opt. A: Pure Appl. Opt. **3**, 267 (2001).

[23] R. Xie and J. Jiang, "Nonlinear optical properties of armchair nanotube," Appl. Phys. Lett. **71**, 1029 (1997).

[24] V. Margulis and T. Sizikova, "Theoretical study of third-order nonlinear optical response of semiconductor carbon nanotubes," Physica B: Condens. Matter **245**, 173 (1998).

[25] H. M. Su, J. T. Ye, Z. K. Tang, and K. S. Wong, "Resonant second-harmonic generation in monosized and aligned single-walled carbon nanotubes," Phys. Rev. B **77**, 125428 (Mar 2008).

[26] L. Vivien, E. Anglaret, D. Riehl, F. Hache, F. Bacou, M. Andrieux, F. Lafonta, C. Journet, C. Goze, M. Brunet, and P. Bernier, "Optical limiting properties of singlewall carbon nanotubes," Opt. Comm. **174**, 271 (2000).

[27] M. Sheik-Bahae, A. Said, T. H. Wei, D. J. Hagan, and E. W. V. Stryland, "Sensitive measurement of optical nonlinearities using a single beam," IEEE J. Quantum Electron. **26**, 760 (Apr. 1990).

[28] O. Muller, Y. Lutz, A. Teissier, J. P. Moeglin, and V. Keller, "Optical limiting behavior of carbon nanotubes exposed to infrared laser irradiations studied by the Z-scan technique," Appl. Opt. **49**, 1097 (2010).

[29] J. Seo, S. Ma, Q. Yang, L. Creekmore, R. Battle, M. Tabibi, H. Brown, A. Jackson, T. Skyles, B. Tabibi, S. Jung, and M. Namkung, "Third-order Optical Nonlinearities of Singlewall Carbon Nanotubes for Nonlinear Transmission Limiting Application," J. Phys.: Conf. Ser. **38**, 37 (2006).

[30] P. Myllyperkio, O. Herranen, J. Rintala, H. Jiang, P. R. Mudimela, Z. Zhu, A. G. Nasibulin, A. Johansson, E. I. Kauppinen, M. Ahlskog, and M. Pettersson, "Femtosecond Four-Wave-Mixing Spectroscopy of Suspended Individual Semiconducting Single-Walled Carbon Nanotubes," ACS Nano **4**, 6780 (2010).

[31] H. Kim, T. Sheps, P. G. Collins, and E. O. Potma, "Nonlinear Optical Imaging of Individual Carbon Nanotubes with Four-Wave-Mixing Microscopy," Nano Lett. **9**, 2991 (2009), pMID: 19637886.

[32] X. Liu, J. Si, B. Chang, G. Xu, Q. Yang, Z. Pan, S. Xie, P. Ye, J. Fan, and M. Wan, "Third-order optical nonlinearity of the carbon nanotubes," Appl. Phys. Lett. **74**, 164 (1999).

[33] C. L. Pint, Y. Xu, M. Pasquali, and R. H. Hauge, "Formation of Highly Dense Aligned Ribbons and Transparent Films of Single-Walled Carbon Nanotubes Directly from Carpets," ACS Nano **2**, 1871 (2008).

[34] L. Ren, C. Pint, L. G. Booshehri, W. D. Rice, X. Wang, D. J. Hilton, K. Takeya, I. Kawayama, M. Tonouchi, R. H. Hauge, and J. Kono, "Carbon Nanotube Terahertz Polarizer," Nano Lett. **9**, 2610 (2009), pMID: 19492842.